Elevated FOXG1 in glioblastoma stem cells cooperates with Wnt/ß-catenin to induce exit 5 from quiescence.

Elevated FOXG1 in glioblastoma stem cells cooperates with Wnt/ß-catenin to induce exit from quiescence.

Authors: Faye L. Robertson, Eoghan O'Duibhir, Ester Gangoso, Raul Bardini Bressan, Harry Bulstrode, Maria-Ángeles Marqués-Torrejón, Kirsty M. Ferguson, Carla Blin, Vivien Grant, Neza Alfazema, Gillian Morrison, and Steven M. Pollard[1]*

Authors Affiliations:

[1] Centre for Regenerative Medicine & Edinburgh Cancer Research UK Centre, Institute for Regeneration and Repair, University of Edinburgh, Edinburgh, UK, EH16 4UU

*** Corresponding author contact:**

Steven Pollard: steven.pollard@ed.ac.uk

Tel: +44 (0)131 6519544

Running title: FOXG1 and Wnt cooperate to stimulate exit from quiescence

Keywords: glioblastoma, neural stem cell, quiescence, cell cycle, FOXG1, GSK3 inhibitor, Wnt signalling, ß-catenin.

Summary

GBM stem cells (GSCs) display phenotypic and molecular features reminiscent of normal neural stem cells, and exhibit a spectrum of cell cycle states (dormant, quiescent, proliferative). However, mechanisms controlling the transition from quiescence to proliferation in both NSCs and GSCs are poorly understood. Elevated expression of the forebrain transcription factor FOXG1 is often observed in GBM. Here, using small molecule modulators and genetic perturbations, we identify a synergistic interaction between FOXG1 and Wnt/ß-catenin signalling. Increased FOXG1 enhances Wnt-driven transcriptional targets enabling highly efficient cell-cycle re-entry from quiescence; however, neither FOXG1 nor Wnt is essential in rapidly proliferating cells. We demonstrate that FOXG1 overexpression supports gliomagenesis *in vivo* and that additional ß-catenin induction drives accelerated tumour growth. These data indicate that elevated FOXG1 cooperates with Wnt signalling to support the transition from quiescence to proliferation in GSCs.

Introduction

Glioblastomas (GBMs) are aggressive, incurable primary brain tumours with a median survival of just over a year [1,2]. Almost all patients suffer fatal relapse following regrowth of the tumour after standard therapies (surgical debulking, chemoradiotherapy and adjuvant chemotherapy). GBMs display inter-tumoral and intra-tumoral heterogeneity at many levels, including genetic drivers, epigenetic landscapes heritable changes in gene expression resulting from mechanisms independent of changes to the genome sequence), and transcriptional circuits [3,4]. However, while genetically heterogeneous, GBMs invariably contain cells with neural stem cell (NSC) identity that are thought to drive tumour growth. GBM stem cells typically express key NSC molecular markers, including neurodevelopmental transcription factors, such as *SOX2*, *SOX9*, *FOXG1* and *POU3F2*. These genes are functionally important in supporting the unconstrained self-renewal that underpins tumour growth [5–8].

GSCs are also heterogeneous in terms of their cell cycle state [3]. Pathologists who score mitotic figures and Ki67 (MIB1) immunoreactivity have noted this for decades. However, with the advent of single-cell transcriptomics, it has become clear that a significant fraction of the tumour cell population exists in a quiescent (slow-cycling) or even dormant (non-cycling) state [3] and that this cell fraction is enriched in tumorigenic cells [9]. Thus, not all cells within the tumour are functionally equivalent in terms of their proliferative output. This heterogeneity must be considered alongside genetic, epigenetic and transcriptional heterogeneity [10], as distinct cell states will likely have different roles in supporting tumour growth and evolution. Current therapeutic strategies focus on targeting actively proliferating GBM cells. However, following surgical debulking, residual cells in the resection margin have quiescent stem cell properties [11]. Given the relative resistance of these populations to chemo- and radiotherapy [12,13], it is perhaps unsurprising that post-chemo/radiotherapy residual tumour cell populations are enriched in quiescent GSCs. These quiescent tumour cells then drive regrowth of the tumour and underpin patient relapse. This has been elegantly demonstrated using genetically engineered mouse models of GBM [14].

Recent advances in our understanding of normal adult NSC quiescence regulation can help guide the exploration of quiescence control in GBM [15]. Equally, regulators of GBM cell cycle control will likely mirror

mechanisms used in normal NSC biology. However, the specific molecular genes and pathways controlling exit from the NSC quiescent state and how these are disrupted in GBM remain unclear. This knowledge will be needed to develop therapeutic approaches rationally designed to eliminate both quiescent and proliferative GSCs.

BMP and EGF pathways promote NSC quiescence and proliferation, respectively, controlling the balance between cell states [16–18]. We and others have shown that elevated FOXG1 contributes to gliomagenesis by attenuating the ability of BMP and related signals to trigger quiescence – in part by suppressing FOXO3 at transcriptional and post-transcriptional levels [19,20]. This suggests FOXG1, which we have shown is not required for GSC proliferation [19], is an important regulator of cell cycle re-entry from quiescence. Moreover, GSCs derived from patient tumours consistently show elevated expression levels of FOXG1 [21,22]. Elevated FOXG1 is, however, insufficient to support efficient exit from quiescence, and the majority of quiescent NSCs engineered to overexpress FOXG1 remain unresponsive to mitogens. Other pathways may therefore restrict competence for mitogen responsiveness and cell cycle re-entry.

Here, to search for pathways that may cooperate with FOXG1 in regulating quiescence exit, we performed a screen of pharmacological small-molecules in NSCs. This led us to uncover a striking synergy between elevated FOXG1 and Wnt signalling. The role of Wnt in GBM has been nebulous. Mutations in components of the Wnt signalling pathway are not significant drivers of GBM and do not trigger glioma formation when mutated in mouse models [23]. NSCs *in vitro* can be expanded in the absence of exogenous Wnt (using just EGF and FGF-2), yet Wnt receptors and ligands are clearly expressed in the adult NSC niche and in GBM tumours, suggesting some functional role [24–27]. Several studies have identified a role for Wnt in modulating tumour stem cell state and, consistently, Wnt pathway activity correlates with poorer patient outcomes [26,28–30].

Our findings suggest that Wnt has a specific role in quiescent GSCs, regulating the exit from quiescence in cooperation with FOXG1. However, when cells are fully proliferative in response to EGF/FGF, Wnt/FOXG1 is dispensable. Wnt/ß-catenin signalling, therefore, has distinct functional roles depending on

the cell cycle status of the cell. This explains why Wnt pathway activity is neither required to sustain proliferative NSCs in vitro nor frequently selected for mutation in GBM. Altogether, our findings suggest that Wnt inhibitors may have value in preventing the reawakening of quiescent GSCs.

Results

A small molecule screen uncovers a GSK3 inhibitor that supports NSC exit from quiescence in the context of FOXG1/SOX2 induction.

We previously reported an *in vitro* model system to explore NSC quiescence; bone morphogenetic protein 4 (BMP4) drives proliferating mouse NSCs into a quiescent astrocyte/NSC-like state that is largely unresponsive to the mitogens EGF/FGF-2 [19]; upon induction of FOXG1 and SOX2 a subset of these cells can become responsive to EGF/FGF-2, re-enter the cell cycle, and re-express markers of radial glia-like NSCs (e.g., *Nestin*, *Fabp7*, *Sox2*, and *Olig2*). However, cell cycle re-entry in this model is not efficient. Most NSCs remain unresponsive and post-mitotic – either dormant or differentiated. We reasoned that there must be other pathways underlying competence for mitogen responsiveness and efficient cell cycle re-entry. Indeed, we previously found that knockout of the cell cycle repressor FOXO3 synergises with FOX/SOX to drive cell cycle re-entry. Here, we used a chemical screen of known pharmacological modulators of key stem cell and cancer pathways to search for additional limiting pathways (StemSelect Library).

We used a previously reported transgenic NSC cell line (FOD3) for this cell-based phenotypic screen, which harbours a TET-inducible FOXG1-2A-SOX2 expression cassette (Figure 1A), plus *Foxo*3 knockout. These cells, therefore, model a key feature of GBM stem cells, namely the excessive levels of FOXG1 and SOX2. The Z' for the screening assay reached 0.6 for FOD3 cells, while it was lower for cells with intact *Foxo3* (Figure S1H). The FOD3 cell line, therefore, provided an optimal cellular model for compound screening. Cells were plated at low density in BMP-4 media for 24 hours and then exposed to EGF/FGF-2 mitogens with doxycycline (Dox) plus library compounds in 96 well format (n=3, Figure 1B). Culture plates were fixed seven days after the addition of compounds. Nuclei were stained with DAPI for quantification, alongside HCS CellMask™ staining to monitor morphological changes (flat spread astrocytic-like appearances, with multiple processes, in quiescence, to bipolar proliferating NSCs, Figure 1B, Figure S1A). Significant hits were defined as compounds which induced cell cycle re-entry with >2-fold increase in cell number (mean nuclei count) over plate median (Figure 1C&D).

Four validated hits were identified; three related to the cAMP pathway (epinephrine, norepinephrine, forskolin; Figure 1C&D). The fourth hit, the glycogen synthase kinase-3 (GSK3) inhibitor, 6-bromoindirubin-3'-oxime (BIO), suggested that Wnt signalling might be a critical co-operating pathway of either FOXG1, SOX2 or FOXO3. Importantly, we tested the effects of these four hits without Dox and found that only BIO triggered proliferation solely in the context of FOXG1/SOX2 overexpression (with Dox) (Figure 1E, Figure S1B&C). These data suggested a potential synergistic interaction between GSK3 inhibition and FOXG1/SOX2 overexpression, supporting highly efficient exit from the quiescent NSC state.

Two distinct GSK inhibitors, BIO and Chiron, cooperate with FOXG1 to stimulate the proliferation of quiescent NSCs.

We next determined if CHIR99021 (Chiron), an alternative GSK3 inhibitor with increased potency and selectivity (An et al. 2012), would give similar results to BIO. Indeed, Chiron was extremely effective at triggering cell cycle re-entry when delivered with FOXG1-SOX2 induction (Figure 2A). Furthermore, given the genetic interactions previously reported between FOXG1 and Wnt during development, we hypothesized that FOXG1 – rather than SOX2, or Foxo3 loss – synergizes with GSK3 inhibition [31,32]. Indeed, in cells with FOXG1 induction alone, but not SOX2, and with intact *FoxO3* (FOXG1-V5 only; F6 cells), we also saw highly efficient exit from quiescence (Figure 2B&C). ~35% of cells in the plus Dox & Chiron condition were driven into the cell cycle, based on EdU incorporation (2hr pulse), compared to <5% of cells in EGF+FGF alone (Figure 2B). Using colony formation assays, we also confirmed the synergistic effects of FOXG1 induction with Chiron (Figure 2D). A high proportion of cells re-entered the cell cycle and generated colonies from their previously quiescent state (Figure 2D). To evaluate the efficiency of colony formation more accurately, cells were plated in serial dilution: 10000, 1000 and 100 cells, respectively. The higher two concentrations each led to a confluent plate at 7-10 days, and 100 cells yielded ~30 colonies (Figure S2E). This ~30% efficiency of colony formation is exceptionally high, especially given that the colony-forming efficiency of proliferative NSCs is typically ~10% (Figure S2F). We conclude that a synergistic effect of elevated FOXG1 and GSK3 inhibition stimulates highly efficient cell cycle re-entry of quiescent NSCs. To confirm that colonies which formed on exposure to Dox+Chiron had NSC properties, we stained them for Nestin and performed serial passage colony assays in EGF+FGF2 media,

demonstrating colony formation after two passages (Figure S2G). Additionally, we differentiated colonies formed after Dox+Chiron exposure with astrocytic and neuronal differentiation protocols (Figure S2H&I). We have previously shown that BMP4 induces a dormant quiescent state, whereas BMP4+FGF2 induces a primed quiescent state [18]. The effect of FOXG1+GSK3 inhibition on exit from quiescence is evident in either model (Figure 2B and Figure S2C). We found that 24hr BMP4 exposure induces a shallower quiescence than 72hr BMP4 exposure, similar to 72hr BMP4+FGF2 (Figure S2A&B), and we use either assay to induce quiescence.

Wnt/ß-catenin signalling pathway synergizes with FOXG1 overexpression to enable efficient exit from quiescence in NSCs

GSK3 is part of the ß-catenin destruction complex, and its inhibition leads to increased stability of ß-catenin, the key downstream effector of the canonical Wnt signalling pathway. However, GSK3 has also been reported to modulate many other signalling pathways, including Notch, Hedgehog and others [33]. To determine if the effects we observed with Chiron are primarily due to activation of the Wnt signalling pathway, we first tested if exogenous Wnt ligands could phenocopy Chiron. Indeed, quantitative analysis of proliferation confirmed that Wnt3a, in the context of FOXG1 induction (plus Dox), could trigger a similar efficiency of cell cycle re-entry and cell morphological changes to Chiron (Figure 3A&B).

We next tested if two different pharmacological inhibitors of Wnt signalling could abrogate the effect of the FOXG1 (Dox) + Chiron: XAV939 is a tankyrase inhibitor which stabilises axin, antagonising Wnt signalling [34]; and ICRT3 is a specific inhibitor of ß-catenin-responsive transcription in the nucleus, downstream of GSK3 [35]. Blockade of the Wnt signalling pathway eliminated the synergistic effects of FOXG1 and Chiron in triggering cell cycle re-entry of NSCs in the quiescent state without significant cell death (Figure 3C&D & Figure S3B). Of note, neither exposure to Wnt3a ligand, nor to the Wnt inhibitors at these doses affected proliferation of actively cycling NSCs (Figure S3A), suggesting that Wnt signalling has a specific role in the exit from quiescence. The above data confirm that FOXG1 and the Wnt signalling pathway cooperate to enable efficient exit from quiescence in NSCs during the initial transition from a quiescent to a cycling state.

We next took a genetic approach to further confirm that the canonical ß-catenin pathway lies downstream of Chiron and Wnt3a. We used a previously reported tamoxifen-inducible-(ERT2)-ß-catenin cassette. With this approach, the addition of 4-hydroxytamoxifen (4-OHT) results in nuclear translocation of N-terminally truncated, stabilised constitutively active ß-catenin; removal of the cassette, via Cre-mediated excision, is reported by activation of GFP expression (Figure 4A) [36,37]. Using plasmid nucleofection, this cassette was stably integrated into F6 (FOXG1-inducible) NSCs. Clonal lines (Dox-inducible FOXG1 plus 4-OHT-inducible ß-catenin; hereafter termed F6BC1 cells) were derived and validated. We confirmed that these F6BC1 NSCs respond to 4-OHT, with inducible Wnt activation, using the TOPflash luciferase transcriptional reporter assay (Figure 4B). Cells were treated transiently with Cre to generate a mixture of ~50% 4-OHT-inducible ß-catenin cells (GFP^-, cassette intact) and non-inducible (GFP^+, cassette excised) cells. This provides an internal negative reference control allowing the investigation of cell-autonomous effects. After BMP4-induced quiescence, cells were returned to mitogens in the presence of Dox and/or Chiron, 4-OHT or both. We scored the % proliferation in the GFP^+ and GFP^- populations (Figure 4C). This experimental system confirmed that ß-catenin induction, in GFP^- cells, phenocopies the effects of Chiron in stimulating cell cycle re-entry and proliferation (Figure 4D&E). GFP^+ cells, lacking the 4-OHT inducible ß-catenin cassette, did not re-enter the cycle efficiently with Dox+4-OHT, suggesting that the effects of FOXG1/ß-catenin are cell autonomous (i.e., there is no rescue of cell cycle entry in adjacent 4-OHT unresponsive cells). As expected, GFP^+ cells remained responsive to Dox+Chiron. We conclude that there is a cooperation between Wnt/ß-catenin signalling and elevated FOXG1 that is sufficient (in the presence of EGF/FGF2) to induce cell cycle re-entry of quiescent NSCs.

Enhanced expression of Wnt target genes is observed in the presence of elevated FOXG1

To interrogate the potential mechanism of the synergy, we initially screened for differences in protein expression of key signalling pathways using reverse phase protein array (RPPA). A timepoint of 3 days after return to EGF/FGF-2 was selected to capture changes occurring prior to the majority of cells re-entering the cell cycle. At this time point, we found only minimal increases in the mitotic marker, phospho-Plk1 (Figure S4B). FOXG1 was upregulated to similar levels by Dox and Dox+Chiron, as determined by

qRT-PCR, confirming that the effect of the addition of Chiron is not due to anomalous further upregulation of FOXG1. (Figure S5A). Hierarchical clustering showed that cells treated with Dox (FOXG1 upregulation) clustered with those treated with the combination of Dox+Chiron. In contrast, cells treated with Chiron clustered with those returned to EGF+FGF alone (Figure 4F), indicating that FOXG1 is the driver of many of the differences in protein expression. The proteins significantly downregulated and upregulated in the Dox+Chiron conditions are shown in Figure S4C. Of note, the four proteins significantly upregulated included known Wnt target genes: c-Myc and Cyclin D1 [38,39], as well as two phospho-Rb proteins downstream of Cyclin D1 (Figure 4F, Figure S4C). c-Myc and phospho-Rb upregulation was confirmed by Western blot (Figure 4G, quantified in Figure S4F&G), with a consistent pattern of upregulation by FOXG1, further increased with Chiron, with some upregulation also observed using Chiron alone. Although these are well-established Wnt targets, they are not exclusively regulated by the Wnt pathway. Accordingly, we conducted Western blotting for Axin2 to confirm the upregulation of Wnt activity by Dox, Chiron and further by Dox+Chiron (Figure S4D&E).

The above data and known roles of Wnt and FOXG1 in other contexts led us to hypothesise that this synergistic pathway involves cell-autonomous changes to transcriptional programs. We, therefore, used the Nanostring mRNA profiling technology to assess the transcriptional levels of key markers associated with known hallmarks of cancer and cancer signalling pathways. This confirmed that transcription of *Myc* and *Axin2* was upregulated by Dox and Chiron, consistent with Wnt pathway activation (Figure 5A&B).

Also noteworthy, we uncovered *Wif1*, a well-established secreted Wnt signalling antagonist (Poggi et al. 2018), as the most significantly repressed gene in the presence of Dox and Chiron (Figure 5). We confirmed that WIF1 protein levels are reduced by elevated FOXG1 (Figure 5D). This reduction in WIF1 levels in the context of FOXG1 could be expected to prime cells to respond to Wnt signalling and becomes functionally relevant at the exit from quiescence. This is consistent with our observation that Dox administration during BMP4 exposure primes cells to exit quiescence in response to Chiron, even where Dox is withdrawn (Figure S5B). Altogether, these observations indicate that elevated FOXG1 enables highly efficient activation of Wnt signalling that supports both transcriptional activation of ß-catenin target genes and

repression of negative regulators of the Wnt signalling pathway. This is consistent with a working model in which elevated FOXG1 in quiescent NSCs increases their responsiveness to Wnt/ß-catenin signalling.

FOXG1 and Wnt cooperate to support tumour progression in a murine model of glioblastoma.

We recently reported that GBM driver mutations (*EGFRvIII*, *Nf1* loss and *Pten* loss) could be efficiently engineered into adult mouse NSCs using CRISPR/Cas9 technology plus PiggyBac transgenesis [40]. The resulting cell lines efficiently induce GBM-like tumours following orthotopic transplantation [40]. Using this strategy, we transformed the F6BC1 cells into a GBM-initiating cell model, wherein we can exogenously control both FOXG1 levels and ß-catenin (see Methods). Tumour formation of F6BC1-NPE cells was confirmed by GFP imaging of freshly dissected whole brains and H&E staining (Figure 6A). We isolated the tumour mass and derived clonal cell lines, confirming that these had the triple combination of GBM driver mutations, tamoxifen-inducible ß-catenin, and Dox-inducible FOXG1-V5 (Figure 6B; Figure S6A). These cell lines were tumour-initiating upon secondary transplantation into the striatum of a fresh cohort of mice.

Using this *in vivo* GBM model system, we were able to test the effects of FOXG1 and ß-catenin on tumourigenesis. At day ten following cell transplantation, half of the mice were given Dox 2mg/ml in drinking water. Tumour formation was monitored using the IVIS luciferase imaging system (Figure 6C). FOXG1 induction in mice treated with Dox was confirmed by staining for the V5 epitope tag (Figure S6A). Importantly, elevated levels of FOXG1 significantly reduced survival (Figure 6D) and increased proliferation markers (Figure S6F&G). This finding is consistent with previously reported patient data showing that high FOXG1 expression is associated with poorer survival outcomes [6], as well as our experimental observations that FOXG1 is required for tumour growth in xenotransplantation GBM models [19].

We next investigated the effect of the combination of FOXG1 upregulation with active Wnt/ß-catenin induction by intraperitoneal (IP) injection of tamoxifen. Increased tumour growth (Figure 6G, S6D) and reduced survival time (Figure 6H) were seen. These data are consistent with our working model that elevated FOXG1 enables enhanced responsiveness to Wnt ligands from the tumour microenvironment *in*

vivo and that ß-catenin can phenocopy these effects. It is likely, however, that ß-catenin induction by tamoxifen adds little to the already high levels of Wnt activity in the tumour microenvironment. ß-catenin expression is seen throughout the mouse brain (Figure S6B) [41]. With FOXG1 induction alone, elevated ß-catenin expression is seen in the tumours, including nuclear ß-catenin expression at earlier time points (Figure 6E, Figure S6E) and this is consistent with findings in human GBM, which express FOXG1 at high levels and show evidence of Wnt pathway activation [26,28–30]. Additionally, Wif1 expression is reduced in the context of FOXG1 induction, consistent with our *in vitro* findings (Figure 6F, Figure S6H). This supports our hypothesis that FOXG1 sensitises cells to Wnt activation; further activation of the pathway accelerates tumour growth and reduces survival. In the context of the *in vitro* findings presented here, we suggest that this may result from increased exit from quiescence by tumour stem cells.

Exit from quiescence was anticipated to be an early event on exposure of cells to high FOXG1 and Wnt signalling, which is challenging to monitor following *in vivo* brain transplantation. Therefore, to interrogate these early events, we used an organotypic *ex vivo* brain slice culture assay to investigate the responses of engrafted tumour cells to FOXG1 overexpression [42]. Tumorigenic cells were labelled with a 4hr EdU pulse before transplantation into brain slices within the striatum. EdU signal is depleted and ultimately lost following rounds of mitotic divisions, so proliferating cells will lose EdU, whereas quiescent cells will retain the label. After three days, following engraftment into the slice, we exposed cells to Dox (FOXG1 overexpression) and compared them to controls with no Dox. On day 7, we found that cells exposed to Dox contained fewer EdU-positive, label-retaining (quiescent) cells than those cultured in mitogens without Dox (Figure 6I&J). Those exposed to Dox demonstrated lower levels of WIF1 expression and the presence of some cells with nuclear ß-catenin expression, which was not seen in the slices with no Dox (Figure 6K, L&M). These findings also indicate that cells with elevated FOXG1 are primed to re-enter the cell cycle and hence contribute to aggressive tumour growth, in keeping with *in vitro* findings (Figure S5B).

The synergy between FOXG1 and GSK3 inhibition is relevant to human patient-derived glioblastoma stem cell lines.

We predicted that findings from our mouse overexpression model would extend to the human GSC context and that a synergy would exist between high FOXG1 expression and GSK3 inhibition. Consistent with published evidence of Wnt activation in human GBM (Figure 7A) [26–30] and FOXG1 overexpression in human GBM [6,21], we confirmed co-localisation of FOXG1 and ß-catenin expression by RNAScope in human GBM tissue isolated at debulking surgery (Figure 7B, Figure S7D). We previously published evidence of cell cycle exit in the majority of human GSCs after eight days continuous exposure to BMP-4 [43]. Accordingly, we treated two patient-derived cell lines, G7 (an adult GSC line) and GBM002 (a paediatric GSC line), along with their CRISPR/Cas9 FOXG1-knockout derivatives [19,44], with BMP4 for eight days. These cells were then re-exposed to EGF+FGF2 +/- Chiron to assess exit from quiescence. Notably, there was a minimal effect of Chiron on the growth of cells in proliferative conditions (Figure 7C). However, after exposure to BMP4, cells with intact FOXG1 treated with Chiron were significantly more likely to re-enter the cell cycle than those returned to EGF+FGF2 without Chiron. This effect was not seen in cells which had ablation of FOXG1 (Figure 7D-F, Figure S7A&B). To assess the synergy in the context of an additional clinically relevant quiescence model, GBM002 cells and the corresponding FOXG1KO line were irradiated with 8Gy and an absence of proliferation was observed. EdU incorporation was assessed at 14 days and was below 10% in almost all wells (Figure 7G). At 14 days, media was supplemented with either Chiron or DMSO, and EdU incorporation was reassessed at days 21 and 28. EdU incorporation and cell number increased with Chiron only in the context of intact FOXG1 (Figure 7H&I, Figure S7E&F). Although further work is needed to characterise quiescent cells in this assay, cells were non-cycling/slowly cycling post-irradiation and, as in a BMP-induced quiescence assay, began proliferating in response to Chiron, only in the context of FOXG1 expression. Taken together, these data suggest that a synergy between FOXG1 and Wnt signalling may be relevant to the regulation of quiescence in human GSCs.

Discussion

Quiescent GSCs are relatively chemo- and radioresistant, and their reactivation leads to tumour recurrence [14,45]. BMP signalling has been shown to regulate quiescence in NSCs, including GSCs [43,46]. Here, using a BMP4-based *in vitro* model of quiescence and unbiased chemical screening, we have been able to uncover a synergistic molecular pathway between FOXG1 and GSK3 inhibition that supports cell cycle re-entry of quiescent NSCs. Our inducible FOXG1 cell lines were designed to model GSC biology, as FOXG1 is typically overexpressed in GSCs relative to NSCs. We show that elevated FOXG1 supports gliomagenesis in our inducible *in vivo* transplantation model, and the FOXG1/Wnt pathway operates in this context. Finally, the synergistic effect of FOXG1 and GSK3 inhibition is operational in human patient-derived GSCs – both adult and paediatric – suggesting disease relevance.

The specific roles of Wnt signalling in NSCs and GBMs still need to be better understood. Our findings help resolve some seemingly contradictory literature, by revealing that Wnt/ß-catenin has a specific cell-context-dependent role in supporting quiescent NSCs/GSCs to re-enter the cell cycle. Our findings are consistent with the function of Wnt in other tissue stem cells, where it provides a locally restricted niche signal that supports the maintenance of stem cell identity [47,48]. A recent study from the Dirks group has shown that Wnt levels are variable in GSCs and that Wnt/ß-catenin, along with Notch, is essential for self-renewal in a subset of cells with a pro-neural signature [49]. In the mouse brain, Austin et al. found that Wnt signalling was dispensable for normal NSC homeostasis, but that ß-catenin stimulation resulted in state-specific effects on NSCs [50]. The roles of Wnt are, therefore highly cell context-dependent – not only in terms of GBM subtype as has been previously shown – but also, as we show here, in the balance between quiescence and proliferation. In future studies, spatial transcriptomics and lineage tracing could help resolve whether the FOXG1/Wnt synergy has niche-specific roles, for example, in the perivascular niche where ß-catenin is expressed at high levels and where quiescent GSCs are found [51].

Using our recently established protocols for the transformation of adult NSCs, and subsequent *in vivo* transplantation, we could generate GBMs in which FOXG1 could be overexpressed. This demonstrated that FOXG1 overexpression leads to accelerated tumour growth and decreased survival, with increased

proliferative GSCs relative to quiescent GSCs. This is consistent with previous *in vitro* findings. FOXG1 leads to increased activation of endogenous Wnt signalling, and additional induction of active ß-catenin further increases the rate of tumour growth and decreases survival. Future studies should focus on further elucidating the biochemical transcriptional mechanism and key downstream effectors of the synergy between FOXG1 and Wnt activity.

The negative impact of FOXG1 overexpression on survival in our mouse model is consistent with previous findings that high FOXG1 mRNA levels in human GBM samples predict poorer overall survival outcomes, and is an exciting corollary to the finding that FOXG1 knockdown in orthotopic GBM transplantation models, results in improved outcomes [6,52] and that FOXG1 knockout in patient-derived GSCs abolishes tumourigenesis [19]. FOXG1 frequently acts as a transcriptional repressor, with evidence of both direct and indirect means of repression [31,53,54]. It is known to regulate the response to TGF-ß signalling, via its action on FoxO-Smad complexes and repression of *p21cip1*, conferring resistance to TGF-ß mediated cytostasis [52]. Given that our data suggested a cell-autonomous mechanism underlying the synergy, it is likely that FOXG1 operates genome-wide, supporting enhanced regulation of a large cohort of Wnt target genes. However, we also identified the secreted factor, WIF1, as a potential downstream effector that may contribute.

In conclusion, our data suggest that elevated FOXG1 may sensitise quiescent GSCs to local Wnt signalling thereby priming subsequent proliferative responses to EGF and FGF signalling pathways (or other RTK pathways). This would explain why high levels of FOXG1 are under positive selection in many GBMs. Furthermore, this model of FOXG1 helps explain why neither FOXG1 nor Wnt signalling are necessary in proliferating GBM cells (as they are specifically required in the context of quiescence). Hence, we predict that suppression of the FOXG1/Wnt pathway would be a poor choice as a first-line therapeutic target in a clinical setting, as it would likely fail to suppress the major proliferative cell component of GBM tumours. Nevertheless, we speculate that the suppression of FOXG1 or the Wnt pathway could suppress the reactivation of the quiescent cells left behind following debulking surgery and chemo/radiotherapy. Wnt

inhibitors may therefore be helpful to prevent the recurrence of GBMs after standard first-line treatments that focus on the proliferative cells.

Limitations of the study

Our reductionist *in vitro* studies provide striking evidence of a synergy between FOXG1 and Wnt signalling in regulating NSC quiescence. Our *in vivo* findings are more modest but likely reflect the high baseline of Wnt ligand in vivo within the tumour microenvironment. Here, we showed a clear effect of FOXG1 overexpression on survival and an additional modest impact of ß-catenin activation. As the interaction between FOXG1 and ß-catenin on exit from quiescence is likely to be an early event in a population for which few markers are validated, it is challenging to interrogate the synergy at a mechanistic level *in vivo*. Future studies could employ functional in vivo experiments with lineage tracing and single cell profiling for detailed assessment of self-renewal and quiescence *in vivo*. As suggested above, spatial transcriptomics are likely to be helpful in identifying niche-specific roles of Wnt and FOXG1 and overcome the limitation of our primarily *in vitro* study. Finally, further work should make use of a broader range of human cell lines to elucidate the precise molecular mechanism of the FOXG1/Wnt synergy, which we suggest may relate to the sequestration of TLE by the FOXG1 Groucho-binding domain.

Acknowledgements

F.L.R. was supported by a CRUK clinical research fellowship (C157/A20919-2).

E.G. was supported by a Postdoctoral Fellowship from Fundación Ramón Areces (Spain)

R.B.B. was supported by a Science Without Borders PhD fellowship (CAPES, Brazil)

S.M.P. is a Cancer research UK Senior Research Fellow (A17368). Patient-derived models and associated data were generated by the Cancer Research UK Centre Accelerator Award (A21922) and this supported G.M.M.

MA-MT was supported by The Brain Tumour Charity Quest for Cures Collaborative Team Award (GN-000358).

We thank Helen Henderson, Marilyn Thomson and Morag Haswell for assistance with cell irradiation and Matthieu Vermeren for assistance with imaging.

Author contributions

Conceptualisation, F.L.R. and S.M.P.; Methodology, F.L.R., E.O'D., E.G., H.B., R.B.B.; Validation, F.L.R.; Formal analysis, F.L.R. and E.O'D.; Investigation, F.L.R., K.M.F., C.B., V.G., N.A., M-A.M-T.; Resources, F.L.R., H.B., R.B.B, E.G., G.M.M.; Writing – original draft F.L.R. and S.M.P.; Writing – review and editing F.L.R. and S.M.P.; Visualisation, F.L.R., E.O'D.; Funding acquisition F.L.R. and S.M.P.; Supervision, G.M.M. and S.M.P.

Figure Legends

Figure 1 | GSK3 inhibition enables efficient cell cycle re-entry in the context of FOXG1/SOX2 overexpression.
(A)&(B) Schematic of the screening process. Cells with conditional FOXG1/SOX2 overexpression and FoxO3 deletion are driven out of cycle by BMP4 treatment. Compounds inducing cell cycle re-entry in the presence of FOXG1/SOX2 induction are screened by assessment of cell number and morphology at 6 days. Created with BioRender. (C) Heatmap of cell number per well at screen end-point, across 4 plates in triplicate, showing 5 potential hits. A scale showing increased cell number above plate median is adopted to highlight wells with clearly high cell number. a=epinephrine, b=forskolin, c=norephinephrine, d=tamoxifen, e=BIO. Controls are in columns 1 and 12 and have cell number below plate median. (D) Scatter plot of cell count expressed as fold change cf. plate median. Means of 3 replicates +/- SD are shown. Red line indicates threshold for calling hits, 2x plate median. Tamoxifen did not validate as a hit (see also Figure S1D&E). (E) Validation of the 4 hits +/- dox; fold change in cell number per well cf. EGF+FGF2+DMSO control. Performed in triplicate. Mean +/- SEM. The concentration of compounds varied, depending on the library concentration: all compounds were used at 1:10000. Refer also to Figure S1. PB: PiggyBac inverted terminal repeat; TRE: tetracycline response element; V5: V5 protein tag; P2A: 2A self-cleaving peptide; IRES: internal ribosome entry site; BSD: blasticidin S deaminase; pA: polyadenylation site; NSCs: neural stem cells; BMP4: bone morphogenetic protein 4; EGF: epidermal growth factor; FGF-2: fibroblast growth factor 2; DMSO: dimethylsulfoxide.

Figure 2 | Highly efficient exit from quiescence into a proliferative state can be achieved by elevating FOXG1 levels and inhibiting GSK3. (A) Increase in FOD3 cell number after BMP4 exposure 24hr and return to EGF+FGF2 +/-Dox and/or BIO or Chiron for 6 days. One-way ANOVA with Dunnett's multiple comparison tests. n=3. Significance shown for comparison to EGF+FGF2. (B) Doxycyline-inducible human FOXG1-V5 cassette. Quantification of cell number in F6 cells (inducible FOXG1 overexpression) in the same assay. One-way ANOVA with Dunnett's multiple comparison tests. n=5 independent replicates, >3 technical replicates each. EdU incorporation in F6 cells by condition. Friedman test. n=8 independent replicates; 15 technical replicates each. Significance shown for comparison to EGF+FGF2. Equivalent assay in cells with inducible SOX2 alone is shown in Figure S1F&G. Mean +/- SEM. (C) Representative images of F6 cells in the same assay. HCS CellMask (green), DAPI (blue). Scale bars 150 μm. (D) Representative images of colony forming assays: F6 cells plated at 5000 cells/well (6 well plate, 5 cells/mm^2) in BMP4 24hr, EGF+FGF2 +/- Dox/Chiron 10 days. Scale bars 2mm. Refer also to Figure S2.

Figure 3 | Elevated Wnt activity synergises with FOXG1 in driving cell cycle re-entry.
(A) Representative images of F6 cells following exposure to BMP4 and return to EGF+FGF2 +/- Wnt3a. HCS CellMask (green), DAPI (blue). (B) Quantification of cell number per well at assay endpoint. Two-

way ANOVA. n=3 independent replicates, 6 technical replicates each. Significance shown for comparison to EGF+FGF2. Mean +/- SEM. (C) Representative images of F6 cells in the BMP4/return to EGF+FGF2 assay in the presence or absence of Wnt inhibitors XAV939 and ICRT3. HCS CellMask (green), DAPI (blue). Scale bars 150μm. DC: +Dox+Chiron (D) Both Wnt inhibitors resulted in a significant reduction in cell number in the cell-cycle re-entry assay. One-way ANOVA. n=6 independent replicates; >5 technical replicates each. Significance shown for comparison to Dox+Chiron condition. Mean +/- SEM. Refer also to Figure S3.

Figure 4 | Highly efficient exit from quiescence into a proliferating state can be achieved by elevating FOXG1 levels and ß-catenin activity. FOXG1 elevation leads to Wnt target gene activation. (A) Schematic of the tamoxifen-inducible constitutively active ß-catenin cassette. (B) TOPflash assay confirms Tcf/lef activation in F6BC1 cells after exposure to the active metabolite of tamoxifen, 4-hydroxytamoxifen (4-OHT) for 48hr. n=4 independent replicates; 6 technical replicates each. Two-tailed Mann Whitney test. (C) Schematic of the assay to assess synergy between FOXG1 and ß-catenin in exit from quiescence. Cre-mediated excision is ~50% efficient, resulting in a mixed population of cells with an intact cassette (and therefore GFP^-) and cells in which the cassette has been excised (GFP^+). These populations are expected to have a differential response to 4-OHT. Created with BioRender. (D) Representative images of F6BC1 cells, transfected with Cre-expression plasmid to excise the ß-catenin cassette in a sub-population of cells, after BMP4 exposure and return to EGF+FGF2 for 4 days. GFP (green), DAPI (blue), EdU (red). (E) EdU incorporation by condition showing that cells with the cassette excised (GFP^+) retain response to Dox+Chiron but not Dox+4-OHT; cells with the cassette (GFP^-) exit quiescence with Dox + either Chiron (GSK3 inhibition) or 4-OHT induction of ß-catenin. Two-way ANOVA with Sidak's multiple comparison tests. n=7 independent replicates; >5 technical replicates each. 4-OHT 1μM. Significance shown for comparison to -Dox -Chiron -4OHT. Mean +/- SEM. Nuclei were delineated and scored using Columbus software algorithms and verified visually. (F) Hierarchical clustering of RPPA data show that F6 cells exposed to Dox, rather than Chiron, cluster with cells exposed to Dox+Chiron. The top upregulated products are Wnt targets or products of Wnt target activity. Asterisks mark proteins demonstrating a significant difference between the EGF+FGF2 and Dox+Chiron conditions. T-tests with Holm-Sidak correction. Independent duplicates; technical triplicates. Additional significant proteins are listed in Figure S4C. (G) Confirmatory Western blot for top hits. GAPDH is used as a loading control. Refer also to Figure S4. LoxP: locus of x-over P1; ERT2: tamoxifen-inducible estrogen receptor ligand binding domain; IRES: internal ribosome entry site; Puro: puromycin resistance sequence; GFP: green fluorescent protein.

Figure 5 | FOXG1 elevation leads to Wnt target gene modulation and repression of Wif1. (A) The most differentially expressed gene in the NanoString dataset is the Wnt inhibitor, *Wif1*, which is downregulated in Dox, Chiron and Dox+Chiron as compared to EGF+FGF2 alone. NanoString was

conducted on RNA extracted from F6 cells after 72 hours in BMP+FGF2 followed by 48 hours in EGF+FGF2 +/- Dox and/or Chiron. Statistics using NSolver Advanced Analysis software as per Wang et al, 2016. Significance shown is for comparison to EGF+FGF2 alone. Performed in independent triplicate. A full list of genes is shown in Table S1. (B) qRT-PCR for Wnt target gene expression in F6 cells after 72 hours in BMP+FGF2 followed by 72 hours in EGF+FGF2 +/- Dox and/or Chiron. One-way ANOVA n=4 independent replicates; 3 technical replicates. Significance shown is for comparison to EGF+FGF2 alone. (C) qRT-PCR analysis of *Wif1* mRNA levels in F6 cells cultured in BMP4 +/- Dox or EGF+FGF2 +/- Dox for 24 hours. n=4 independent replicates; technical duplicates. Two-tailed T-test. (B&C) Expression values were normalised to *Gapdh* and shown relative to the expression in EGF+FGF-2 -Dox (in which log2(FC) = 0). Y axis represents log2(Fold change), equivalent to -ddCt value. All graphs show mean +/- SEM. (D) Western blot analysis of WIF1 expression in F6 cells +/- Dox for 24h grown in NS cell media (EGF/FGF). GAPDH is used as a loading control. Refer also to Figure S5.

Figure 6 | FOXG1 upregulation in GBM *in vivo/ex vivo* leads to increased ß-catenin, reduced Wif1, reduced quiescent cell fraction and shorter survival. Additional induction of ß-catenin leads to accelerated tumour growth and further reduces survival time.(A) GFP-expressing tumours form after orthotopic transplantation of F6BC1NPE cells. Haematoxylin and eosin (H&E) staining confirms GBM histology. (B) Western blot of clonal cell lines generated from tumours, showing gain of EGFRvIII, loss of NF-1 and PTEN, partial in the bulk population pre-transplantation and complete in the clonal lines derived after transplantation. GAPDH is used as a loading control. EM3 and EM4 refer to the mice from which tumour was taken and the clonal lines derived. (C) Schematic of *in vivo* experiment. F6BC1NPE cells (EM4 clone 6) were transplanted orthotopically into the brains of NSG mice. After 10 days, mice were given Dox 2mg/ml in 5% glucose, or 5% glucose alone, as drinking water. IVIS imaging was conducted weekly. Created with BioRender. (D) Survival curve showing significant reduction in survival for mice given Dox. Log-rank (Mantel Cox) test. n=6 per group. (E) Representative immunohistochemistry images from tumours of mice given Dox or no Dox showing increased ß-catenin expression in the Dox condition. DAPI, blue. GFP, green. ß-catenin, red. Scale bars 50μm. See also Figure S6E. (F) Representative immunohistochemistry images from tumours of mice given Dox or no Dox and culled at 21 days, showing reduced Wif1 expression in the Dox condition. DAPI, blue. GFP, green. Wif1, red. Scale bars 50μm. Quantified in Figure S6H. (G) Quantification of IVIS signal over time in two groups of mice given either Dox alone or Dox + IP Tamoxifen (see also Figure S6C&D) shows faster growth in the Dox+Tamoxifen group as compared to Dox alone. Non-linear regression analysis n=9 per group. As the mice with the largest tumours in the Dox+Tam group had been culled by 5 weeks, last recorded values are carried over (from 3 or 4 weeks, widening the SEM but allowing comparison between groups). Mean +/- SEM. (H) Survival curve showing reduction in survival for mice given Dox+Tam as compared to Dox alone. Log-rank (Mantel Cox) test. n=13 per group. (I) Representative images from the engrafted tumour regions in organotypic slice culture exposed to EGF+FGF2 for 3 days, to allow engraftment, then EGF+FGF2 +/- Dox for a further

4 days, showing label retaining cells. EdU (LRC – label retaining cells), red. DAPI, blue. Scale bars 50μm. (J) Quantification of label retaining cell fraction in the slice culture assay. One-way ANOVA with Tukey's multiple comparison tests. Performed in duplicate. Mean +/- SEM. (K) Immunohistochemistry for Wif1 shows increased signal and cytoplasmic staining after 7 days in EGF+FGF2 alone cf. 3 days. This is lost in the presence of Dox (FOXG1 overexpression). Wif1, red. DAPI, blue. Scale bars 50μm. (L) In the presence of Dox, a proportion of cells express nuclear ß-catenin in keeping with Wnt pathway activation. ß-catenin, red. DAPI, blue. Scale bars 50μm. (M) Quantification of proportion of cells in organotypic slice culture expressing nuclear or cytoplasmic ß-catenin. Performed in duplicate and measured over 6 fields at 40x. Refer also to Figure S6.

Figure 7 | The synergy between FOXG1 and Wnt signaling is relevant to two human glioma cell lines.

(A) In situ hybridisation for Ctnnb1 in an adult GBM specimen (Ivy GBM Atlas Project) – *Ctnnb1* is expressed in tumour tissue, most markedly in perivascular regions. Scale bars 800μm and 200μm (expanded image). (B) Representative images of RNAScope performed on human GBM tissue (G313). DAPI, blue; *FoxG1* mRNA, red; *Ctnnb1* (ß-catenin) mRNA, yellow. Scale bars 50μm. (C) Growth curve for G7 cells in EGF+FGF2 +/- Chiron 3μM n=3. (D) Representative images of G7 cells after BMP-induced quiescence (8 days) and return to mitogens for 4 days showing response to Chiron only where FOXG1 is intact. Blue - DAPI, Orange - HCS CellMask. Scale bars 150μm. (E&F) Quantification of EdU incorporation in G7 and G7 FOXG1 KO cells (E) and in GBM002 and GBM002 KO cells (F), expressed as fold change cf. EGF+FGF2 alone, showing that Chiron drives exit from quiescence in a dose-dependent manner, only in the context of intact FOXG1. Two-way ANOVA with Sidak's multiple comparison tests. (E) n=6 independent replicates; >6 technical replicates each. (F) n=3 independent replicates; 15 technical replicates (G) EdU incorporation in GBM002 and GBM002 FOXG1KO cells 14 days after irradiation with 8Gy n=42 technical replicates in 2 independent experiments. (H&I) Impact of Chiron on EdU incorporation in GBM002 and GBM002KO cells. Cells, plated at 30 cells/mm2, were irradiated with 8Gy at Day 0. At day 14, either Chiron or DMSO were added to media. At days 21 or 28, a 2hr EdU pulse was performed. (H) Fold change in EdU incorporation at 28 days, as compared with 14 days, in Chiron or DMSO control for the parental and FOXG1KO cell lines. Data are expressed as fold change to account for slight variations in baseline EdU and between two independent experiments. Two-way ANOVA, p=0.0499. (I) Data

551 expressed as ratio of EdU incorporation in Chiron:DMSO over time. Linear regression analysis p=0.0118.

552 Graphs show mean +/- SEM. Refer also to Figure S7.

553

554

STAR METHODS

RESOURCE AVAILABILITY

Lead contact

Further information and requests for resources should be directed to, and will be fulfilled by, the lead contact, Steven Pollard (steven.pollard@ed.ac.uk)

Materials availability

All reagents generated in this study (including cell lines and plasmids) are available on request from S.M.P.

Data and code availability

Nanostring data have been deposited at the University of Edinburgh DataShare repository and are publicly available as of the date of publication. DOIs are listed in the key resources table.

This paper does not report original code.

Any additional information required to reanalyse the data reported in this paper is available from the lead contact on request.

EXPERIMENTAL MODEL AND STUDY PARTICIPANT DETAILS

Mice and *in vivo* procedures

All animal work on NSG (NOD-SCID gamma; non-obese diabetic, severe combined immunodeficiency with null mutation in IL2Rγ) mice was performed in accordance with protocols approved by Home Office UK guidelines in a designated facility under a project license to S.M.P. (PC0395462) at the University of Edinburgh. Mice were maintained on a regular diet in a pathogen-free facility on a 12-hr light/dark cycle with unlimited access to food and water. For NSCs transplants, 6-8 week old male mice were anaesthetised with inhalation vapour mix of oxygen at 2l/min and isofluorane (Zoetis UK Ltd: VM 42058/4195) at 4% for induction and at 2-3% for maintenance on a stereotaxic frame. Stereotactic coordinates used were 1.5mm lateral, 0.6mm anterior to the bregma and 2.5mm deep. NSCs concentrated (~5×10^4/µl) were injected in a volume of 2µl with a Hamilton syringe at 0.2µl/min. Mice were given doxycycline 2mg/ml in drinking water with 5% glucose, or 5% glucose alone. Where tamoxifen was administered, mice were given intraperitoneal

tamoxifen 120mg/kg or sunflower oil vehicle on day 1 (after transplantation on day 0). Monitoring of tumour growth in vivo was conducted by bioluminescence imaging 20 minutes after D-Luciferin (potassium salt) subcutaneous injection (50 mg/kg, Cayman chemical) using the IVIS Lumina LT Series III (PerkinElmer) instrument. Bioluminescence signals were analysed using Living Image Software v.4.5.2 (Perkin Elmer). Animals culled due to symptoms or signs of deterioration were included in survival analysis.

METHOD DETAILS

Cell culture

NSCs were isolated from the adult SVZ and maintained *in vitro* in presence of EGF and FGF-2 and laminin. Cells were cultured at 37°C and 5% CO2 and grown on uncoated tissue culture plastic. Dissociation was performed using accutase (Sigma). Cells were passaged 1:6 to 1:8, or media changed as appropriate, every 3-4 days. For colony forming assays NSCs were plated at low density (5000 cells per well-6 multiwell plate, 5 cells/mm^2) in BMP4 for 24 hours or BMP4+FGF2 for 72 hours, when media were changed to fresh self-renewal media. For 96 well plate assays, cells were plated at 1000 cells per well (30 cells/mm^2). For the screen, plating was performed using the Multidrop Combi reagent dispenser (ThermoFisher 5840300); compound addition was performed using the CyBio Felix liquid handler (AnalytikJena). For induction of quiescence, BMP4 for 24 hours or BMP4+FGF2 for 72 hours were used and led to equivalent levels of EdU incorporation (Figure S2A&B). BMP4+FGF2 for 72 hours was the predominant quiescence assay [18]. Self-renewal media: Mouse and human neural stem NSCs and GSCs were grown under serum-free conditions in DMEM F-12 supplemented with N2 and B27, penicillin-streptomycin, 1 µg/ml Laminin, 10 ng/ml EGF and 10 ng/ml FGF [56,58]. Selection media contained puromycin, hygromycin or blasticidin. BMP4 (Peprotech, AF-120-05ET-100), FGF2 (Peprotech, # 100-18b) EGF (Peprotech (#315-09). Astrocyte differentiation assay: 10% FCS for 5 days. Neuronal differentiation assay: withdrawal of EGF for 24hr followed by withdrawal of FGF-2 for 7 days. Growth curves were generated using an IncuCyte live-cell imaging system. DMSO was used as a control in assays where compounds were added to media, unless otherwise stated. Details of the G7 and GBM002 cell lines and FOXG1 knockout have previously been published [19,44].

Cell transfection

Design and construction of CRISPR sgRNAs is described in [59]. The Amaxa (Lonza) nucleofection system was used. The pulse programs used were X005 (human cells), T030 (mouse PiggyBac) and DN100 (mouse random integration and CRISPR). In each case 1-2 million cells were transfected. For inducible PiggyBac constructs, a total of 6-12ug DNA was used, comprising pBASE, pCAG-Tet3G (PTre3G promoter, Clontech) and pDEST-TetOn (from pCAG Tet-On 3G Transactivator, Clontech) vector in 1:1:2 ratios. For CRISPR targeting, guide RNAs (x2), targeting vector (where appropriate) and Cas9 nickase were transfected in a 1:1:1:2 ratio. For single transfection NPE transformation, 1.5 million cells were transfected with 4.2ug DNA comprising cas9-mCherryNF1guide sequence x2, PTENgRNA sequence x2, PB-PyCAG-EGFRviii, PB-CAG-GFP-LUC-Ires-Bsd, pCMV-hyPBase in a 1:1:1:1:1:1:1 ratio. For random integration, 2 million cells were transfected with 1ug of linearised plasmid DNA. The tamoxifen-inducible(ERT2)-ß-catenin plasmid was a kind gift from the laboratory of Prof Austin Smith.

Immunocytochemistry

Cells were fixed with 4% paraformaldehyde for 10 min, incubated in blocking buffer (10% normal goat serum and 0.2% Triton X-100 in 0.1M phosphate buffer saline) for 30 min, and incubated overnight at 4°C with the indicated primary antibodies: FOXG1 (1:3, Pollard lab), GFP (1:1000, Abcam 13970), Sox2 (1:100, Millipore 5603), V5 tag (1:1000, eBioscience 14-6796-82), ß-catenin (1:500, BD 610154), TuJ1 (1:250 Biolegend 801202), Nestin (1:10 Developmental Studies Hybridoma Bank), GFAP (1:100 Biolegend 28294). After several washes with PBS, immunoreactivity was detected with the appropriate Alexa Fluor-conjugated (Life Technologies) secondary antibody (1:1000). Cells were counterstained with 4′,6′, -diamidino-2-phenylindole (DAPI) and mounted with Fluorsave (Calbiochem). HCS CellMask (ThermoFisher H32714 green, H32713 orange) was used as per manufacturers' instructions. EdU detection Click-it Thermo Fisher C10337 and TUNEL assay Click-it Thermo Fisher C10245 kits were used. Images were taken and analysed using Confocal (Leica SP8, 3 and 5 detectors), Nikon TiE, or the PerkinElmer Operetta high content imaging system (with Harmony and Columbus software for image analysis). Quantification of signal intensity or of nuclei count, GFP or EdU positivity was conducted using Columbus algorithms or ImageJ. For Columbus algorithms, nuclei were selected using pre-set software

parameters, selected objects were then subjected to exclusion criteria based on size, roundness, signal intensity and contact with the edge of the imaged field. Cytoplasm was delineated using pre-set software parameters and objects in contact with the edge of the imaged field were excluded. Selected objects were visually verified in a minimum of 25% of imaged fields in a minimum of 10% of imaged wells in each plate.

Immunohistochemistry

Brains were fixed in 4% PFA overnight at 4ºC, then rinsed several times with PBS and stored in PBS +0.05% sodium azide. For histopathology procedures, brains were transferred into 70% ethanol and then embedded in paraffin for processing. 10mm coronal slices were prepared for hematoxylin and eosin (H&E) staining. For immunohistochemistry of fixed brain tissue, 50µm vibratome slices were transferred into a 24-well plate. Slices were incubated at room temperature for 30 min in blocking solution (0.2% Triton X-100 and 3% Goat Serum). Primary antibodies were incubated overnight at 4C as follows: Ki-67 (1:100 Thermo Fisher MA5-14520), GFP (1:300 Abcam13970), ß-catenin (1:500, BD 610154), WIF1 (1:500, Abcam 186845). After three washes with PBS, slices were incubated with appropriate Alexa Fluor secondary antibodies (1:1000, Life technologies) and DAPI (1:2000, Sigma D9542) for 2 hours. Slices were washed three times and were mounted on a slide with FluoroSave™ Reagent (345789, Calbiochem). Slices were examined with a confocal microscope (Leica TCS SP8).

Slice co-culture assay

Young adult mouse brains (5-6 weeks old) were removed, sliced and cultured [42]. Cells growing *in vitro* were deposited in the striatum of the brain slices. Label retaining cells were labeled using EdU and, after being deposited in organotypic slice culture, were exposed to EGF+FGF2 for 3 days then EGF+FGF2 +/- Dox for a further 4 days. Co-cultures were fixed with PFA 4% and stained with primary and secondary antibodies [42] and EdU cell proliferation click it kit (ThermoFisher). Samples were examined with a confocal microscope (Leica TCS SP8). Quantification was conducted using ImageJ software.

Western Immunoblotting

Immunoblotting was performed using standard protocols. Antibodies were diluted in 5% milk powder inTBS Tween 20 0.1%, and protein detection was carried out with HRP-coupled secondary antibodies and X-ray films. The following primary antibodies were used Axin2 (1:1000, Abcam 109307), SOX2 (1:400, R&D MAB2018), Phospho-Rb (S780) (1:500, Abcam 47763), c-MYC (1:1000, Abcam 32072), FOXG1 (1:50, hybridoma clone 17B12, Pollard lab), WIF1 (1:500, Abcam 186845), NF1 (1:500; Santa Cruz sc-67), PTEN (1:1000; CST 9556), phospho-EGFR Tyr1068 (1:1000; CST 3777), GAPDH (1:40000; ThermoFisher, 6C5), Actin (1:1000; Santa Cruz sc-1616). Quantification of band signal and normalisation to GAPDH signal was performed using ImageJ software and Excel.

Topflash assay

Cells were transfected with a Renilla luciferase plasmid and either the TOPflash plasmid, containing the TCF/LEF-Firefly luciferase expression construct (7 copies of the TCF/LEF transcriptional activator site upstream of firefly luciferase, a gift from Randall Moon via Addgene) or the FOPflash control, in which the TCF/LEF sites are mutated and cannot be activated by ß-catenin. Renilla activity was recorded as a control for transfection efficiency and results were normalised to Renilla activity prior to determining the ratio between TOPflash and FOPflash firefly luciferase activity. The Promega Dual Luciferase Assay was conducted according to manufacturers' instructions.

Quantitative real-time RT-PCR

RNA was extracted using the RNeasy spin column kit (Qiagen), plus DNase treatment to eliminate gDNA. cDNA was generated with SuperScript III (Invitrogen), and quantitative RT-PCR was performed using Taqman Universal PCR Master Mix (Applied Biosystems). The following Taqman assays (Life Technologies) were used: Axin2 (Mm00443610_m1), FoxG1 (Mm02059886_s1), FOXG1 (Hs01850784_s1), Myc (Mm00487804_m1), Wif1 (Mm00442355_m1).

RPPA

Samples were prepared using Lysis Buffer: 1% Triton X-100,50 mM HEPES, pH 7.4, 150 mM NaCl, 1.5 mM MgCl2, 1 mM EGTA, 100 mM NaF, 10 mM Na pyrophosphate, 1 mM Na3VO4, 10% glycerol,

supplemented with cOmplete ULTRA protease inhibitor and PhosSTOP phosphatase inhibitor cocktails (Roche), on ice. Sample Buffer: 40% Glycerol,8% SDS, 0.25 M Tris-HCL, pH 6.8. Before use, 2-mercaptoethanol was added at 1/10 of the volume. Clarified supernatants in biological triplicate were adjusted to 2 mg/mL concentration and printed onto nitrocellulose-coated slides (Grace Bio-Labs) in a dilution series (four serial 2-fold dilutions) in technical triplicate using an Aushon2470 arrayer (Aushon Biosystems). Slides were blocked, probed with validated primary antibodies and detected with DyLight 800-conjugated secondary anti-bodies (New England BioLabs). Slides were read using an InnoScan 710-IR scanner (Innopsys) and quantified using Mapix (Innopsys). Relative fluorescence intensities were normalized to respective FastGreen-stained spots (total protein), and data were computationally analyzed as previously described [60].

Nanostring

RNA was extracted from cells, and gDNA eliminated, using the RNeasy Mini Kit (Qiagen, 74104). The Nanostring PanCancer Pathways panel was used. Hybridization, purification and imaging on the nCounter system were conducted in accordance with manufacturers' protocols. Raw protein count data were processed by applying background thresholding and content normalization in NanoString nSolver 4.0.

Creation of the F6BC1NPE line

F6BC1 cells were transfected using the DN 100 program of a 4D nucleofection system (Lonza). 1.5 x 10^6 cells were resuspended in 100µl of SG transfection solution (Lonza). We delivered, via a single transfection, CRISPR gRNAs for *Nf1* and *Pten* deletion (+mCherry reporter), alongside PiggyBac CAG-EGFRvIII (+ hygromycin selectable), GFP and firefly luciferase (+ blasticidin selectable), to F6BC1 cells. Cells were sorted for dual GFP and Cherry positivity and subsequently exposed to hygromycin (100 µg/ml hygromycin) for 5 days and blasticidin (5 µg/ml) for 6 days sequentially to recover fully transfected cells. These pool of cells (200K) were transplanted into the striatum of 6 x NSG mice and in five of these mice we were able to see aggressive tumours by IVIS bioluminescence imaging of live animals.

RNAScope

RNAScope was conducted on 5μm slices of FFPE tissue prepared from human GBM samples obtained at the time of primary surgery. The RNAScope Multiplex Fluorescent Kit v2 Assay (ACD) was conducted in accordance with manufacturer's instructions. Slices were examined with an inverted fluorescence microscope (Leica). G313 was obtained at surgery by Mr Paul Brennan.

Cell irradiation

Cells were cultured in adherent monolayer and irradiated in a Gammacell 40 Exactor (Best Theratronics) or sham irradiated. When removed from the incubator, culture plates were sealed with Parafilm (Bemis) until returned.

QUANTIFICATION AND STATISTICAL ANALYSIS

Screening data were analysed, and data visualisations created, with Spotfire (Tibco) and StratoMineR (Core Life Analytics). RPPA data were assessed using Cluster 3.0 and Java TreeView 3.0 and graphs created in GraphPad Prism 8. nSolver software was used for Nanostring analysis. Statistical analyses were performed in GraphPad Prism 8. Biological replicates were considered as different passage numbers of the same cell line plated in independent experiments. Mean and SEM are plotted unless otherwise stated. Statistical tests used are indicated in the figure legends. p values are denoted as follows * <0.05, ** <0.01, *** <0.001, **** <0.0001, ns > 0.05.

Declaration of Interests

The authors declare no competing interests.

References

1. Stupp, R., Mason, W.P., van den Bent, M.J., Weller, M., Fisher, B., Taphoorn, M.J.B., Belanger, K., Brandes, A.A., Marosi, C., Bogdahn, U., et al. (2005). Radiotherapy plus concomitant and adjuvant temozolomide for glioblastoma. N. Engl. J. Med. *352*, 987–996.

2. Marenco-Hillembrand, L., Wijesekera, O., Suarez-Meade, P., Mampre, D., Jackson, C., Peterson, J., Trifiletti, D., Hammack, J., Ortiz, K., Lesser, E., et al. (2020). Trends in glioblastoma: outcomes over time and type of intervention: a systematic evidence based analysis. J. Neurooncol. *147*, 297–307.

3. Patel, A.P., Tirosh, I., Trombetta, J.J., Shalek, A.K., Gillespie, S.M., Wakimoto, H., Cahill, D.P., Nahed, B.V., Curry, W.T., Martuza, R.L., et al. (2014). Single-cell RNA-seq highlights intratumoral heterogeneity in primary glioblastoma. Science *344*, 1396–1401.

4. Wang, Q., Hu, B., Hu, X., Kim, H., Squatrito, M., Scarpace, L., deCarvalho, A.C., Lyu, S., Li, P., Li, Y., et al. (2017). Tumor Evolution of Glioma-Intrinsic Gene Expression Subtypes Associates with Immunological Changes in the Microenvironment. Cancer Cell *32*, 42-56.e6.

5. Bachoo, R.M., Maher, E.A., Ligon, K.L., Sharpless, N.E., Chan, S.S., You, M.J., Tang, Y., DeFrances, J., Stover, E., Weissleder, R., et al. (2002). Epidermal growth factor receptor and Ink4a/Arf: convergent mechanisms governing terminal differentiation and transformation along the neural stem cell to astrocyte axis. Cancer Cell *1*, 269–277.

6. Verginelli, F., Perin, A., Dali, R., Fung, K.H., Lo, R., Longatti, P., Guiot, M.-C., Del Maestro, R.F., Rossi, S., di Porzio, U., et al. (2013). Transcription factors FOXG1 and Groucho/TLE promote glioblastoma growth. Nat. Commun. *4*, 2956.

7. Suvà, M.L., Rheinbay, E., Gillespie, S.M., Patel, A.P., Wakimoto, H., Rabkin, S.D., Riggi, N., Chi, A.S., Cahill, D.P., Nahed, B.V., et al. (2014). Reconstructing and reprogramming the tumor-propagating potential of glioblastoma stem-like cells. Cell *157*, 580–594.

8. Sachamitr, P., Ho, J.C., Ciamponi, F.E., Ba-Alawi, W., Coutinho, F.J., Guilhamon, P., Kushida, M.M., Cavalli, F.M.G., Lee, L., Rastegar, N., et al. (2021). PRMT5 inhibition disrupts splicing and stemness in glioblastoma. Nat. Commun. *12*, 1–17.

9. Deleyrolle, L.P., Harding, A., Cato, K., Siebzehnrubl, F.A., Rahman, M., Azari, H., Olson, S., Gabrielli, B., Osborne, G., Vescovi, A., et al. (2011). Evidence for label-retaining tumour-initiating cells in human glioblastoma. Brain *134*, 1331–1343.

10. Nassar, D., and Blanpain, C. (2016). Cancer Stem Cells: Basic Concepts and Therapeutic Implications. Annu. Rev. Pathol. *11*, 47–76.

11. Glas, M., Rath, B.H., Simon, M., Reinartz, R., Schramme, A., Trageser, D., Eisenreich, R., Leinhaas, A., Keller, M., Schildhaus, H.-U., et al. (2010). Residual tumor cells are unique cellular targets in glioblastoma. Ann. Neurol. *68*, 264–269.

12. Bao, S., Wu, Q., McLendon, R.E., Hao, Y., Shi, Q., Hjelmeland, A.B., Dewhirst, M.W., Bigner, D.D., and Rich, J.N. (2006). Glioma stem cells promote radioresistance by preferential activation of the DNA damage response. Nature *444*, 756–760.

13. Beier, D., Schulz, J.B., and Beier, C.P. (2011). Chemoresistance of glioblastoma cancer stem cells--much more complex than expected. Mol. Cancer *10*, 128.

14. Xie, X.P., Laks, D.R., Sun, D., Ganbold, M., Wang, Z., Pedraza, A.M., Bale, T., Tabar, V., Brennan, C., Zhou, X., et al. (2022). Quiescent human glioblastoma cancer stem cells drive tumor initiation, expansion, and recurrence following chemotherapy. Dev. Cell *57*, 32-46.e8.

15. Obernier, K., and Alvarez-Buylla, A. (2019). Neural stem cells: origin, heterogeneity and regulation in the adult mammalian brain. Development *146*. 10.1242/dev.156059.

16. Mira, H., Andreu, Z., Suh, H., Lie, D.C., Jessberger, S., Consiglio, A., San Emeterio, J., Hortigüela, R., Marqués-Torrejón, M.A., Nakashima, K., et al. (2010). Signaling through BMPR-IA regulates quiescence and long-term activity of neural stem cells in the adult hippocampus. Cell Stem Cell *7*, 78–89.

17. Martynoga, B., Mateo, J.L., Zhou, B., Andersen, J., Achimastou, A., Urbán, N., van den Berg, D., Georgopoulou, D., Hadjur, S., Wittbrodt, J., et al. (2013). Epigenomic enhancer annotation reveals a key role for NFIX in neural stem cell quiescence. Genes Dev. *27*, 1769–1786.

18. Marqués-Torrejón, M.Á., Williams, C.A.C., Southgate, B., Alfazema, N., Clements, M.P., Garcia-Diaz, C., Blin, C., Arranz-Emparan, N., Fraser, J., Gammoh, N., et al. (2021). LRIG1 is a gatekeeper to exit from quiescence in adult neural stem cells. Nat. Commun. *12*, 1–15.

19. Bulstrode, H., Johnstone, E., Marques-Torrejon, M.A., Ferguson, K.M., Bressan, R.B., Blin, C., Grant, V., Gogolok, S., Gangoso, E., Gagrica, S., et al. (2017). Elevated FOXG1 and SOX2 in glioblastoma enforces neural stem cell identity through transcriptional control of cell cycle and epigenetic regulators. Genes Dev. *31*, 757–773.

20. Dali, R., Verginelli, F., Pramatarova, A., Sladek, R., and Stifani, S. (2018). Characterization of a FOXG1:TLE1 transcriptional network in glioblastoma-initiating cells. Mol. Oncol. *12*, 775–787.

21. Engström, P.G., Tommei, D., Stricker, S.H., Ender, C., Pollard, S.M., and Bertone, P. (2012). Digital transcriptome profiling of normal and glioblastoma-derived neural stem cells identifies genes associated with patient survival. Genome Med. *4*, 76.

22. Sturm, D., Witt, H., Hovestadt, V., Khuong-Quang, D.-A., Jones, D.T.W., Konermann, C., Pfaff, E., Tönjes, M., Sill, M., Bender, S., et al. (2012). Hotspot mutations in H3F3A and IDH1 define distinct epigenetic and biological subgroups of glioblastoma. Cancer Cell *22*, 425–437.

23. Gibson, P., Tong, Y., Robinson, G., Thompson, M.C., Currle, D.S., Eden, C., Kranenburg, T.A., Hogg, T., Poppleton, H., Martin, J., et al. (2010). Subtypes of medulloblastoma have distinct developmental origins. Nature *468*, 1095–1099.

24. Adachi, K., Mirzadeh, Z., Sakaguchi, M., Yamashita, T., Nikolcheva, T., Gotoh, Y., Peltz, G., Gong, L., Kawase, T., Alvarez-Buylla, A., et al. (2007). β-Catenin Signaling Promotes Proliferation of Progenitor Cells in the Adult Mouse Subventricular Zone. Stem Cells *25*, 2827–2836.

25. Kalani, M.Y.S., Cheshier, S.H., Cord, B.J., Bababeygy, S.R., Vogel, H., Weissman, I.L., Palmer, T.D., and Nusse, R. (2008). Wnt-mediated self-renewal of neural stem/progenitor cells. Proc. Natl. Acad. Sci. U. S. A. *105*, 16970–16975.

26. Liu, C., Tu, Y., Sun, X., Jiang, J., Jin, X., Bo, X., Li, Z., Bian, A., Wang, X., Liu, D., et al. (2011). Wnt/beta-Catenin pathway in human glioma: expression pattern and clinical/prognostic correlations. Clin. Exp. Med. *11*, 105–112.

27. Kaur, N., Chettiar, S., Rathod, S., Rath, P., Muzumdar, D., Shaikh, M.L., and Shiras, A. (2013). Wnt3a mediated activation of Wnt/β-catenin signaling promotes tumor progression in glioblastoma. Mol. Cell. Neurosci. *54*, 44–57.

28. Zhang, N., Wei, P., Gong, A., Chiu, W.-T., Lee, H.-T., Colman, H., Huang, H., Xue, J., Liu, M., Wang, Y., et al. (2011). FoxM1 promotes β-catenin nuclear localization and controls Wnt target-gene expression and glioma tumorigenesis. Cancer Cell *20*, 427–442.

29. Rheinbay, E., Suvà, M.L., Gillespie, S.M., Wakimoto, H., Patel, A.P., Shahid, M., Oksuz, O., Rabkin, S.D., Martuza, R.L., Rivera, M.N., et al. (2013). An aberrant transcription factor network essential for Wnt signaling and stem cell maintenance in glioblastoma. Cell Rep. *3*, 1567–1579.

30. Portela, M., Venkataramani, V., Fahey-Lozano, N., Seco, E., Losada-Perez, M., Winkler, F., and Casas-Tintó, S. (2019). Glioblastoma cells vampirize WNT from neurons and trigger a JNK/MMP signaling loop that enhances glioblastoma progression and neurodegeneration. PLoS Biol. *17*, e3000545.

31. Yao, J., Lai, E., and Stifani, S. (2001). The winged-helix protein brain factor 1 interacts with groucho and hes proteins to repress transcription. Mol. Cell. Biol. *21*, 1962–1972.

32. Buscarlet, M., Perin, A., Laing, A., Brickman, J.M., and Stifani, S. (2008). Inhibition of cortical neuron differentiation by Groucho/TLE1 requires interaction with WRPW, but not Eh1, repressor peptides. J. Biol. Chem. *283*, 24881–24888.

33. Doble, B.W., and Woodgett, J.R. (2003). GSK-3: tricks of the trade for a multi-tasking kinase. J. Cell Sci. *116*, 1175–1186.

34. Huang, S.-M.A., Mishina, Y.M., Liu, S., Cheung, A., Stegmeier, F., Michaud, G.A., Charlat, O., Wiellette, E., Zhang, Y., Wiessner, S., et al. (2009). Tankyrase inhibition stabilizes axin and antagonizes Wnt signalling. Nature *461*, 614–620.

35. Watanabe, K., and Dai, X. (2011). Winning WNT: race to Wnt signaling inhibitors. Proc. Natl. Acad. Sci. U. S. A. *108*, 5929–5930.

36. Lo Celso, C., Prowse, D.M., and Watt, F.M. (2004). Transient activation of beta-catenin signalling in adult mouse epidermis is sufficient to induce new hair follicles but continuous activation is required to maintain hair follicle tumours. Development *131*, 1787–1799.

37. Kim, H., Wu, J., Ye, S., Tai, C.-I., Zhou, X., Yan, H., Li, P., Pera, M., and Ying, Q.-L. (2013). Modulation of β-catenin function maintains mouse epiblast stem cell and human embryonic stem cell self-renewal. Nat. Commun. *4*, 1–11.

38. He, T.C., Sparks, A.B., Rago, C., Hermeking, H., Zawel, L., da Costa, L.T., Morin, P.J., Vogelstein, B., and Kinzler, K.W. (1998). Identification of c-MYC as a target of the APC pathway. Science *281*, 1509–1512.

39. Shtutman, M., Zhurinsky, J., Simcha, I., Albanese, C., D'Amico, M., Pestell, R., and Ben-Ze'ev, A. (1999). The cyclin D1 gene is a target of the beta-catenin/LEF-1 pathway. Proc. Natl. Acad. Sci. U. S. A. *96*, 5522–5527.

40. Gangoso, E., Southgate, B., Bradley, L., Rus, S., Galvez-Cancino, F., McGivern, N., Güç, E., Kapourani, C.-A., Byron, A., Ferguson, K.M., et al. (2021). Glioblastomas acquire myeloid-affiliated transcriptional programs via epigenetic immunoediting to elicit immune evasion. Cell *184*, 2454-2470.e26.

41. Lein, E.S., Hawrylycz, M.J., Ao, N., Ayres, M., Bensinger, A., Bernard, A., Boe, A.F., Boguski, M.S., Brockway, K.S., Byrnes, E.J., et al. (2007). Genome-wide atlas of gene expression in the adult mouse brain. Nature *445*, 168–176.

42. Marques-Torrejon, M.A., Gangoso, E., and Pollard, S.M. (2018). Modelling glioblastoma tumour-host cell interactions using adult brain organotypic slice co-culture. Dis. Model. Mech. *11*. 10.1242/dmm.031435.

43. Carén, H., Stricker, S.H., Bulstrode, H., Gagrica, S., Johnstone, E., Bartlett, T.E., Feber, A., Wilson, G., Teschendorff, A.E., Bertone, P., et al. (2015). Glioblastoma Stem Cells Respond to Differentiation Cues but Fail to Undergo Commitment and Terminal Cell-Cycle Arrest. Stem Cell Reports *5*, 829–842.

44. Bressan, R.B., Southgate, B., Ferguson, K.M., Blin, C., Grant, V., Alfazema, N., Wills, J.C., Marques-Torrejon, M.A., Morrison, G.M., Ashmore, J., et al. (2021). Regional identity of human neural stem cells determines oncogenic responses to histone H3.3 mutants. Cell Stem Cell *28*, 877-893.e9.

45. Chen, J., Li, Y., Yu, T.-S., McKay, R.M., Burns, D.K., Kernie, S.G., and Parada, L.F. (2012). A restricted cell population propagates glioblastoma growth after chemotherapy. Nature *488*, 522–526.

46. Sachdeva, R., Wu, M., Johnson, K., Kim, H., Celebre, A., Shahzad, U., Graham, M.S., Kessler, J.A., Chuang, J.H., Karamchandani, J., et al. (2019). BMP signaling mediates glioma stem cell quiescence and confers treatment resistance in glioblastoma. Sci. Rep. *9*, 14569.

47. Clevers, H., Loh, K.M., and Nusse, R. (2014). Stem cell signaling. An integral program for tissue renewal and regeneration: Wnt signaling and stem cell control. Science *346*, 1248012.

48. Nusse, R., and Clevers, H. (2017). Wnt/β-Catenin Signaling, Disease, and Emerging Therapeutic Modalities. Cell *169*, 985–999.

49. Rajakulendran, N., Rowland, K.J., Selvadurai, H.J., Ahmadi, M., Park, N.I., Naumenko, S., Dolma, S., Ward, R.J., So, M., Lee, L., et al. (2019). Wnt and Notch signaling govern self-renewal and differentiation in a subset of human glioblastoma stem cells. Genes Dev. *33*, 498–510.

50. Austin, S.H.L., Gabarró-Solanas, R., Rigo, P., Paun, O., Harris, L., Guillemot, F., and Urbán, N. (2021). Wnt/β-catenin signalling is dispensable for adult neural stem cell homeostasis and activation. Development *148*. 10.1242/dev.199629.

51. Gilbertson, R.J., and Rich, J.N. (2007). Making a tumour's bed: glioblastoma stem cells and the vascular niche. Nat. Rev. Cancer *7*, 733–736.

52. Seoane, J., Le, H.-V., Shen, L., Anderson, S.A., and Massagué, J. (2004). Integration of Smad and forkhead pathways in the control of neuroepithelial and glioblastoma cell proliferation. Cell *117*, 211–223.

53. Hanashima, C., Shen, L., Li, S.C., and Lai, E. (2002). Brain factor-1 controls the proliferation and differentiation of neocortical progenitor cells through independent mechanisms. J. Neurosci. *22*, 6526–6536.

54. Zaret, K.S., and Carroll, J.S. (2011). Pioneer transcription factors: establishing competence for gene expression. Genes Dev. *25*, 2227–2241.

55. Hennika, T., Hu, G., Olaciregui, N.G., Barton, K.L., Ehteda, A., Chitranjan, A., Chang, C., Gifford, A.J., Tsoli, M., Ziegler, D.S., et al. (2017). Pre-Clinical Study of Panobinostat in Xenograft and Genetically Engineered Murine Diffuse Intrinsic Pontine Glioma Models. PLoS One *12*, e0169485.

56. Pollard, S.M., Yoshikawa, K., Clarke, I.D., Danovi, D., Stricker, S., Russell, R., Bayani, J., Head, R., Lee, M., Bernstein, M., et al. (2009). Glioma stem cell lines expanded in adherent culture have tumor-specific phenotypes and are suitable for chemical and genetic screens. Cell Stem Cell *4*, 568–580.

57. Thorvaldsdóttir, H., Robinson, J.T., and Mesirov, J.P. (2013). Integrative Genomics Viewer (IGV): high-performance genomics data visualization and exploration. Brief. Bioinform. *14*, 178–192.

58. Conti, L., Pollard, S.M., Gorba, T., Reitano, E., Toselli, M., Biella, G., Sun, Y., Sanzone, S., Ying, Q.-L., Cattaneo, E., et al. (2005). Niche-independent symmetrical self-renewal of a mammalian tissue stem cell. PLoS Biol. *3*, e283.

59. Bressan, R.B., Dewari, P.S., Kalantzaki, M., Gangoso, E., Matjusaitis, M., Garcia-Diaz, C., Blin, C., Grant, V., Bulstrode, H., Gogolok, S., et al. (2017). Efficient CRISPR/Cas9-assisted gene targeting enables rapid and precise genetic manipulation of mammalian neural stem cells. Development *144*, 635–648.

914 60. Byron, A. (2017). Clustering and Network Analysis of Reverse Phase Protein Array Data. Methods
915 Mol. Biol. *1606*, 171–191.

STAR METHODS

KEY RESOURCES TABLE

REAGENT or RESOURCE	SOURCE	IDENTIFIER
Antibodies		
Actin	Santa Cruz	Cat#: sc-1616
Axin2	Abcam	Cat#: 109307
ß-catenin	BD	Cat#: 610154
c-MYC	Abcam	Cat#: 32072
FOXG1	In house	N/a
GAPDH	ThermoFisher	Cat#: 6C5
GFAP	Biolegend	Cat#: 28294
GFP	Abcam	Cat#: 13970
Ki67	ThermoFisher	Cat#: MA5-14520
Nestin	Developmental Studies Hybridoma Bank	Cat#: rat-401
NF1	Santa Cruz	Cat#: sc-67
Phospho-EGFR Tyr1068	Cell Signaling Technology	Cat#: 3777
Phospho-Rb (S780)	Abcam	Cat#: 47763
PTEN	Cell Signaling Technology	Cat#: 9556
SOX2 (IF)	Millipore	Cat#: 5603
SOX2 (WB)	R&D	Cat#: MAB2018
TuJ1	Biolegend	Cat#: 801202
V5	eBioscience	Cat#: -6796-82
WIF1	Abcam	Cat#: 186845
Biological samples		

Glioma tissue and derived cells	Glioma Cellular Genetics Resource, CRUK, UK	http://gcgr.org.uk
Chemicals, peptides, and recombinant proteins		
DMEM/HAMS-F12	Sigma	Cat#: D8437
Pen/Strep	Gibco	Cat#:15140-122
Glucose	Sigma Aldrich	Cat#: G8644
MEM-NEAA (100X)	Gibco	Cat#: 11140-035
BSA Solution	Gibco	Cat#:15260-037
Beta Mercaptoethanol	Gibco	Cat#: 31350-010
B27 Supplement (50X)	LifeTech/Gibco	Cat#: 17504-044
N2 Supplement (100X)	LifeTech/Gibco	Cat#: 17502-048
Recombinant Mouse EGF	Peprotech	Cat#: 315-09
Recombinant Human FGF	Peprotech	Cat#: 100-18b
Laminin	Cultrex	Cat#: 3446-005-01
Accutase	Sigma Aldrich	Cat#: A6964
Glutamine	Gibco	Cat#: 25030-021
Mouse Recombinant BMP4	Peprotech	Cat#: 5020-BP
Potassium Chloride	Sigma Aldrich	Cat#: P3911
Methanol	Fisher Scientific	Cat#: 13298233
DAPI	Thistle Scientific	Cat#: 30-45-01
SG Cell Line Transfection Kit	Lonza	Cat#: V4XC-3032
Blasticidin	Invivogen	Cat#: ANT-BL-1
Hygromycin B	Life Technologies	Cat#: 10687010
DMSO	Sigma Aldrich	Cat#: 276855
dNTPs	Thermo Scientific	Cat#: R0191
LongAMP Taq Polymerase	NEB	Cat#: M0323
Paraformaldehyde Powder 95%	Sigma	Cat#: 158127
Triton X-100	Merck Life Sciences	Cat#: X-100

Goat Serum	Sigma Aldrich	Cat#: G6767
Milk Powder	Marvel	N/A
Tween 20	Cambridge Bioscience	Cat#: TW0020
SuperScript III	Invitrogen	Cat#: 18080093
Sodium Azide	Fisher Scientific	Cat#: 12615117
PBS Tablets	Sigma Aldrich	Cat#: P4417
Ethanol	VWR	Cat#: 20821-330
FluoroSave Reagent	Calbiochem	Cat#: 345789
DNase	Sigma Aldrich	Cat#: 101041590001
FBS	Gibco	Cat#: 10270-106
Taqman Universal PCR Master Mix	Applied Biosystems	Cat#: 4305719
D-Luciferin potassium salt	Cambridge Bioscience	Cat#: CAY14681
SuperG Blocking Buffer	Grace Bio Labs	Cat#: 105100
IRDye 800CW Streptavidin	LI-COR Biosciences	Cat#: 926-32230
cOmplete ULTRA protease inhibitor	Roche	Cat#: 05056489001
PhosSTOP phosphatase inhibitor	Roche	Cat#: 04906837001
HCS CellMask	ThermoFisher	Cat#: H32714, H32713
Recombinant mouse Wnt3a	R&D	Cat#: 1324-WN-002
CHIR99021	Axon Medchem	Cat#: 1386
Critical commercial assays		
RNeasy Mini Kit	Qiagen	Cat#: 74104
Click-iT EdU Cell Proliferation Kit for Imaging	ThermoFisher	Cat#: C10377
Click-iT TUNEL Alexa Fluor Imaging Assay	ThermoFisher	Cat#: C10245
Dual Luciferase Reporter Assay System	Promega	Cat#: E1910
Mouse Gapdh Taqman gene expression assay	ThermoFisher	Mm99999915_g1
Mouse Axin2 Taqman gene expression assay	ThermoFisher	Mm00443610_m1
Mouse Foxg1 Taqman gene expression assay	ThermoFisher	Mm02059886_s1
Human FOXG1 Taqman gene expression assay	ThermoFisher	Hs01850784_s1

Mouse Myc Taqman gene expression assay	ThermoFisher	Mm00487804_m1
Mouse Wif1 Taqman gene expression assay	ThermoFisher	Mm00442355_m1
RNAScope Multiplex Fluorescent Kit v2 Assay	ACD	
nCounter PanCancer Pathways Panel	Nanostring	
Deposited data		
Nanostring	This manuscript	Edinburgh DataShare https://doi.org/10.7488/ds/3835
Experimental models: Cell lines		
FOD3	[19]	N/a
S15	[19]	N/a
F6	[19]	N/a
F6BC1	This paper	N/a
F6BC1NPE and derived lines	This paper	N/a
pGBM002 (HSJD-GBM-002)	[55]	N/a
aGBM7 (G7)	[56]	N/a
GCGR Human Glioma Stem Cells	This paper, Glioma Cellular Genetics Resource, CRUK, UK	N/a
Experimental models: Organisms/strains		
Mouse: NSG (NOD-scid-gamma)	Charles River (original source, colony bred in house)	Cat#: 614NSG
Oligonucleotides		
Refer to Table S2.	This manuscript.	N/A
Recombinant DNA		
Cas9D10A-2A-GFP	Addgene	Cat#: 44720

PiggyBAC transposase	Austin Smith, University of Cambridge	N/A
Gateway pDONR™221	ThermoFisher	Cat#: 12536017
M50 Super 8x TOPflash	Addgene	Cat#: 12456
M51 Super 8x FOPflash	Addgene	Cat#: 12457
ERT2-ß-catenin	Austin Smith, University of Cambridge	N/A
Software and algorithms		
Incucyte® Base Software	Essen Bioscience	https://www.essenbioscience.com/en/products/incucyte/
Fiji/ImageJ	Open Source	https://imagej.net/Fiji
BioRender	BioRender	https://biorender.com/
IGV (version 2.8.2)	[57]	http://software.broadinstitute.org/software/igv/
GraphPad Prism 9.0	GraphPad Software, Inc	https://www.graphpad.com/
Spotfire	Tibco	https://www.tibco.com/products/tibco-spotfire
StratoMineR	Core Life Analytics	https://corelifeanalytics.com/

Columbus	PerkinElmer	https://www.perkinelmer.com/uk/product/image-data-storage-and-analysis-system-columbus
Harmony	PerkinElmer	https://www.perkinelmer.com/uk/product/harmony-4-9-office-license-hh17000010
Living Image Software v.4.5.2	PerkinElmer	https://resources.perkinelmer.com/corporate/content/lst_software_downloads/release-notes-li-4.5.2.pdf
Mapix	Innopsys	https://www.innopsys.com/product/corporate/mapix-software/
Cluster 3.0	Open Source	http://bonsai.hgc.jp/~mdehoon/software/cluster/
Java TreeView 3.0	Open Source	https://jtreeview.sourceforge.net/
nSolver 4.0	Nanostring	https://nanostring.com/products/analysis-solutions/nsolver-advanced-analysis-software/
Other		

RESOURCE AVAILABILITY

Lead contact

Further information and requests for resources should be directed to, and will be fulfilled by, the lead contact, Steven Pollard (steven.pollard@ed.ac.uk)

Materials availability

All reagents generated in this study (including cell lines and plasmids) are available on request from S.M.P.

Data and code availability

Nanostring data have been deposited at the University of Edinburgh DataShare repository and are publicly available as of the date of publication. DOIs are listed in the key resources table.

This paper does not report original code.

Any additional information required to reanalyse the data reported in this paper is available from the lead contact on request.

Figure 1

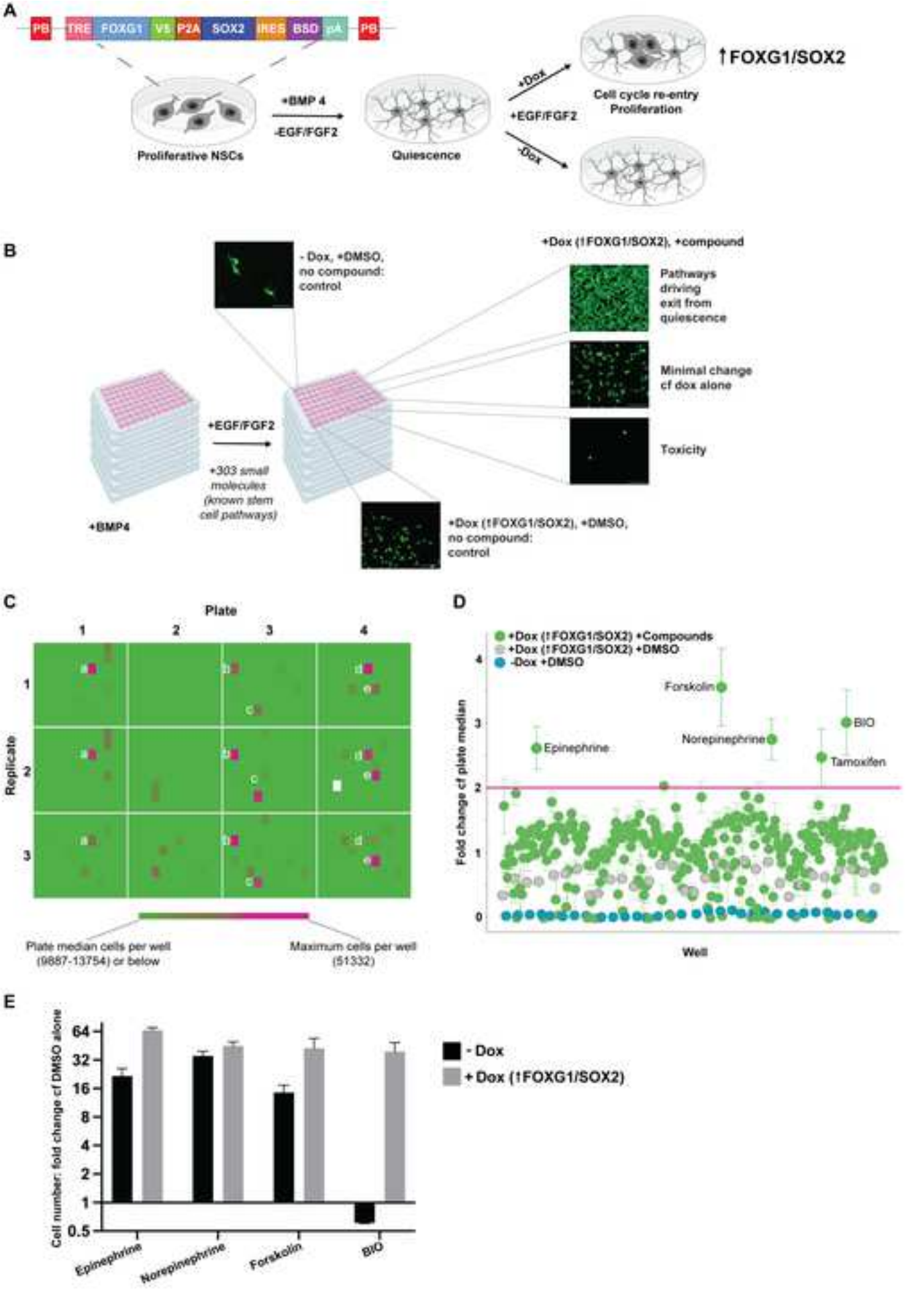

Figure 2

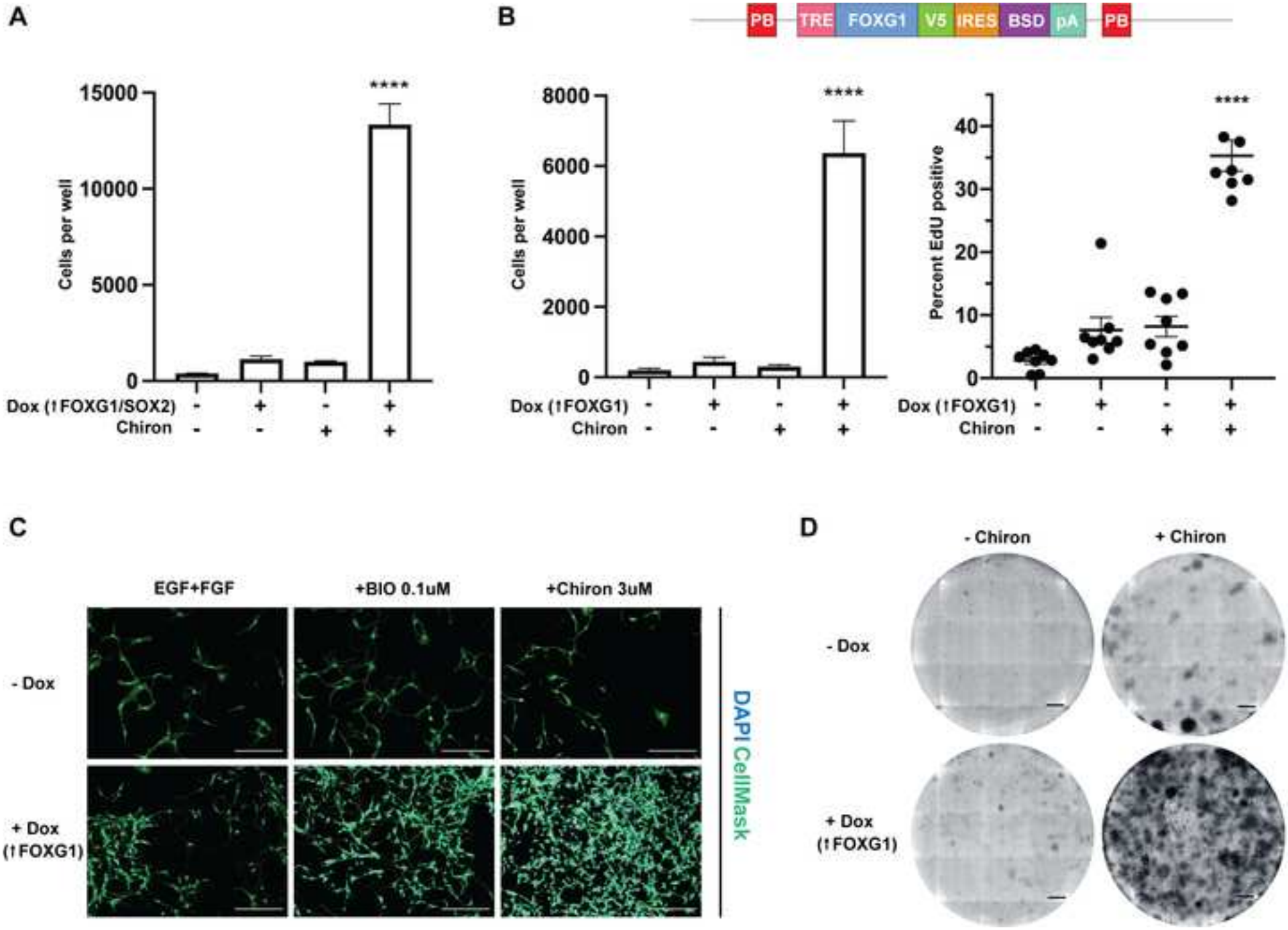

Figure 3

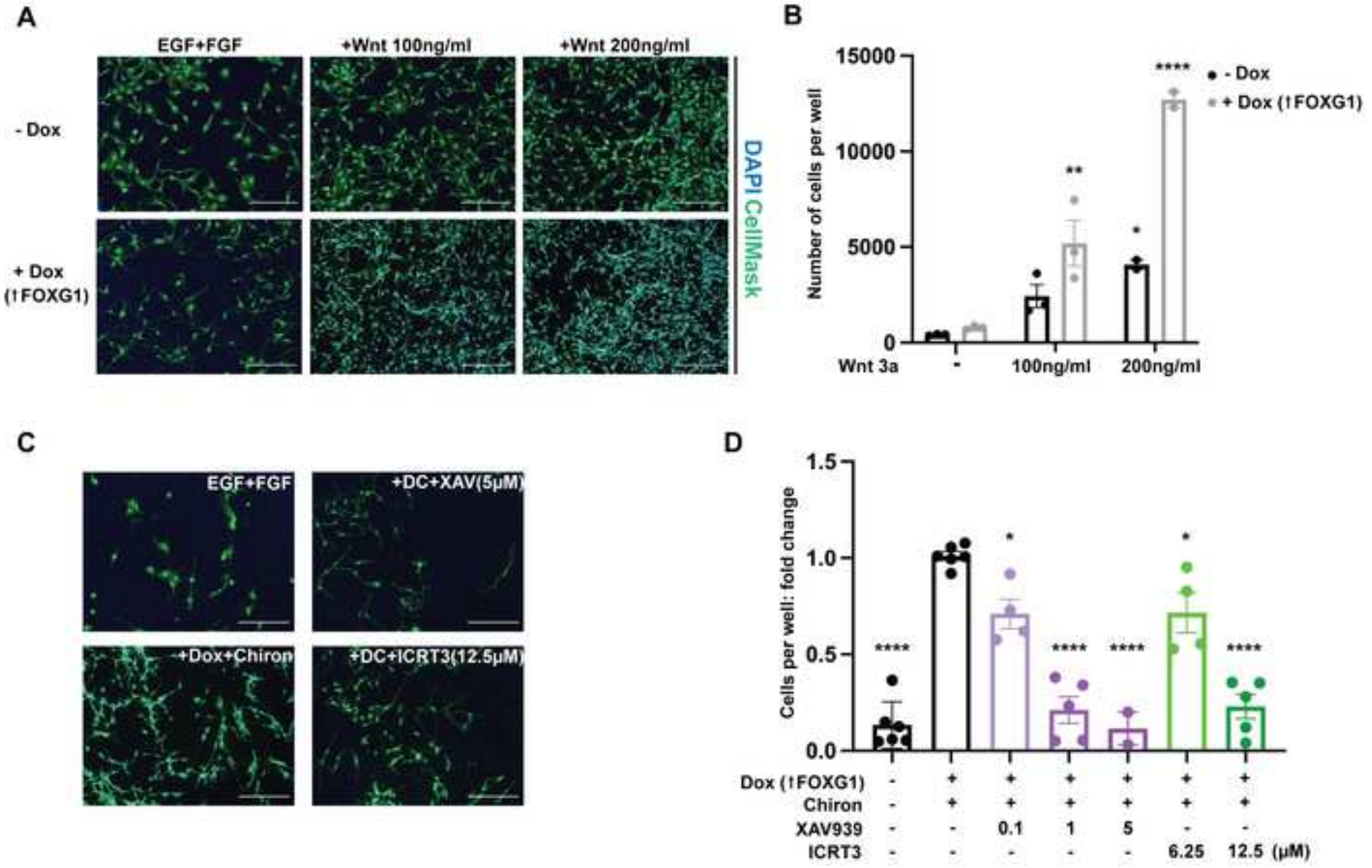

Figure 4

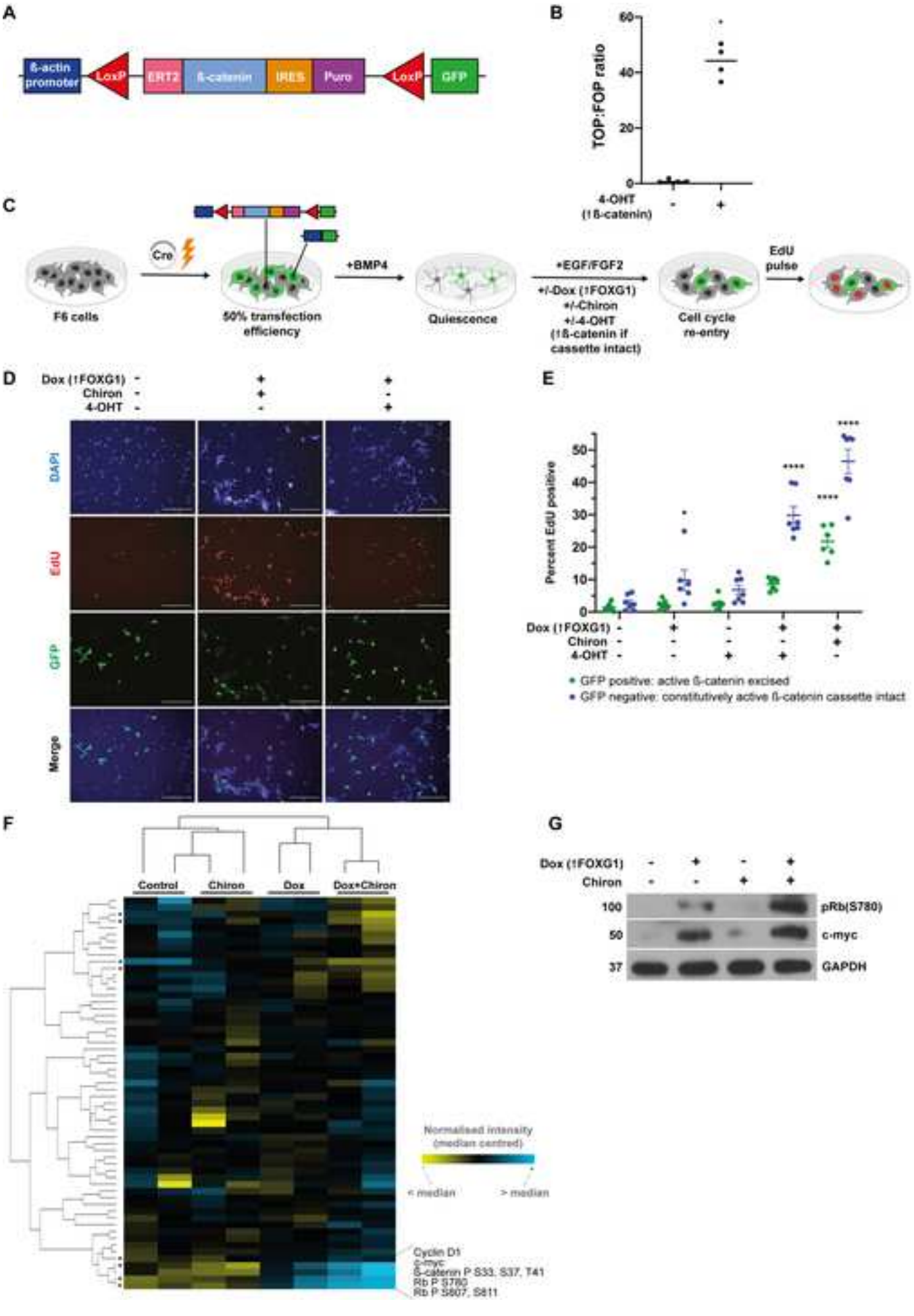

Figure 5

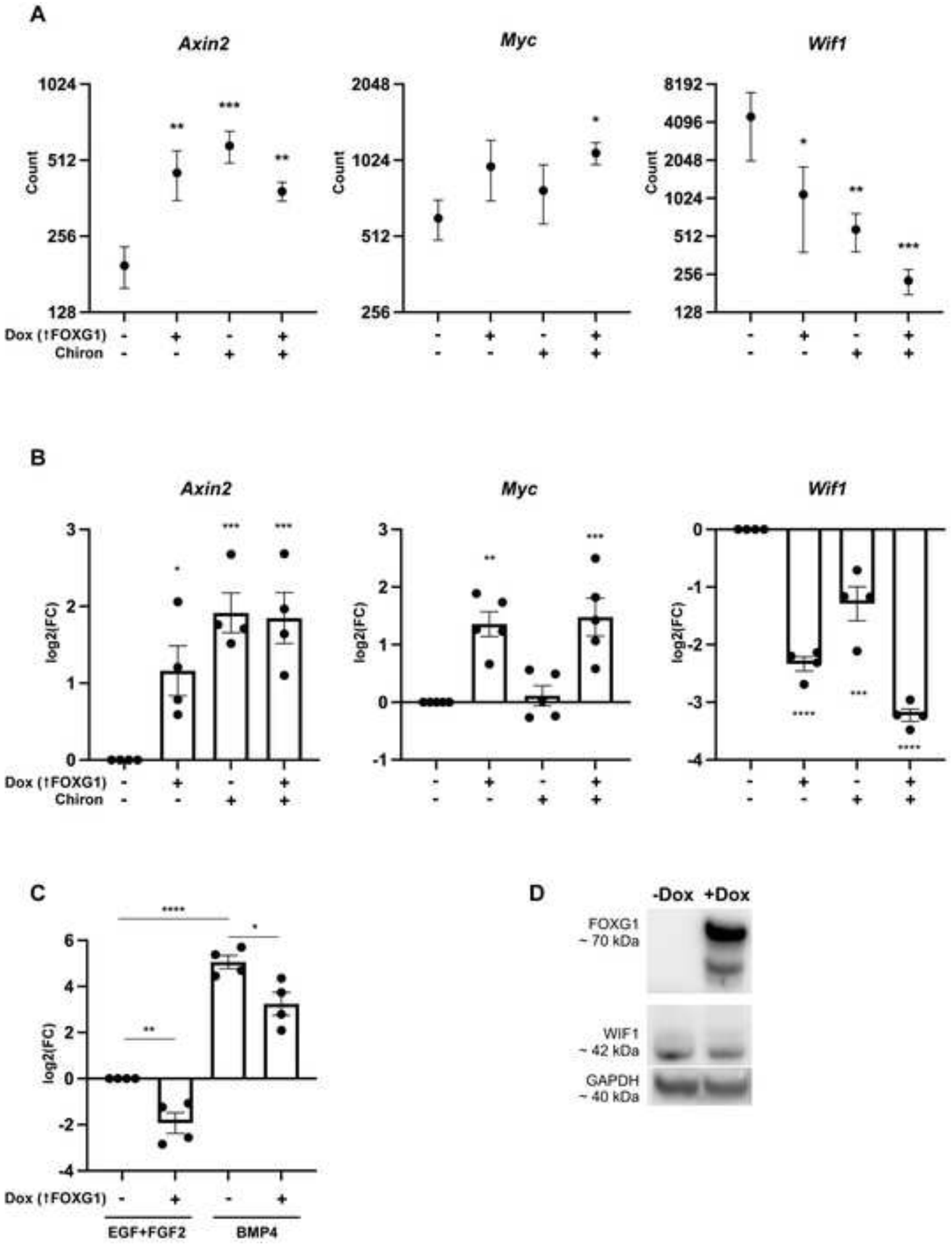

Figure 6

Click here to access/download;Figure;Figure6.tif

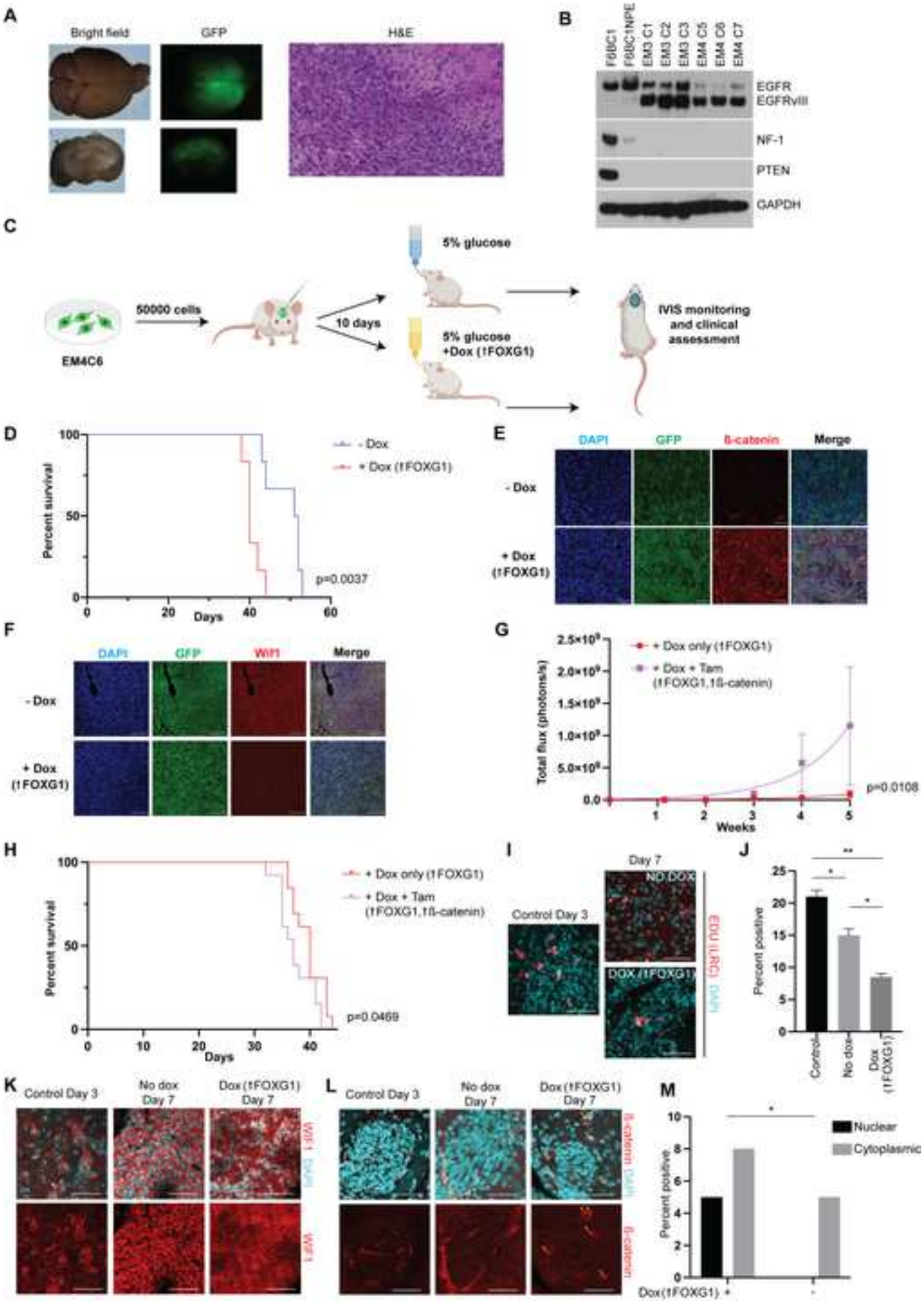

Figure 7

Click here to access/download;Figure;Figure7.tif

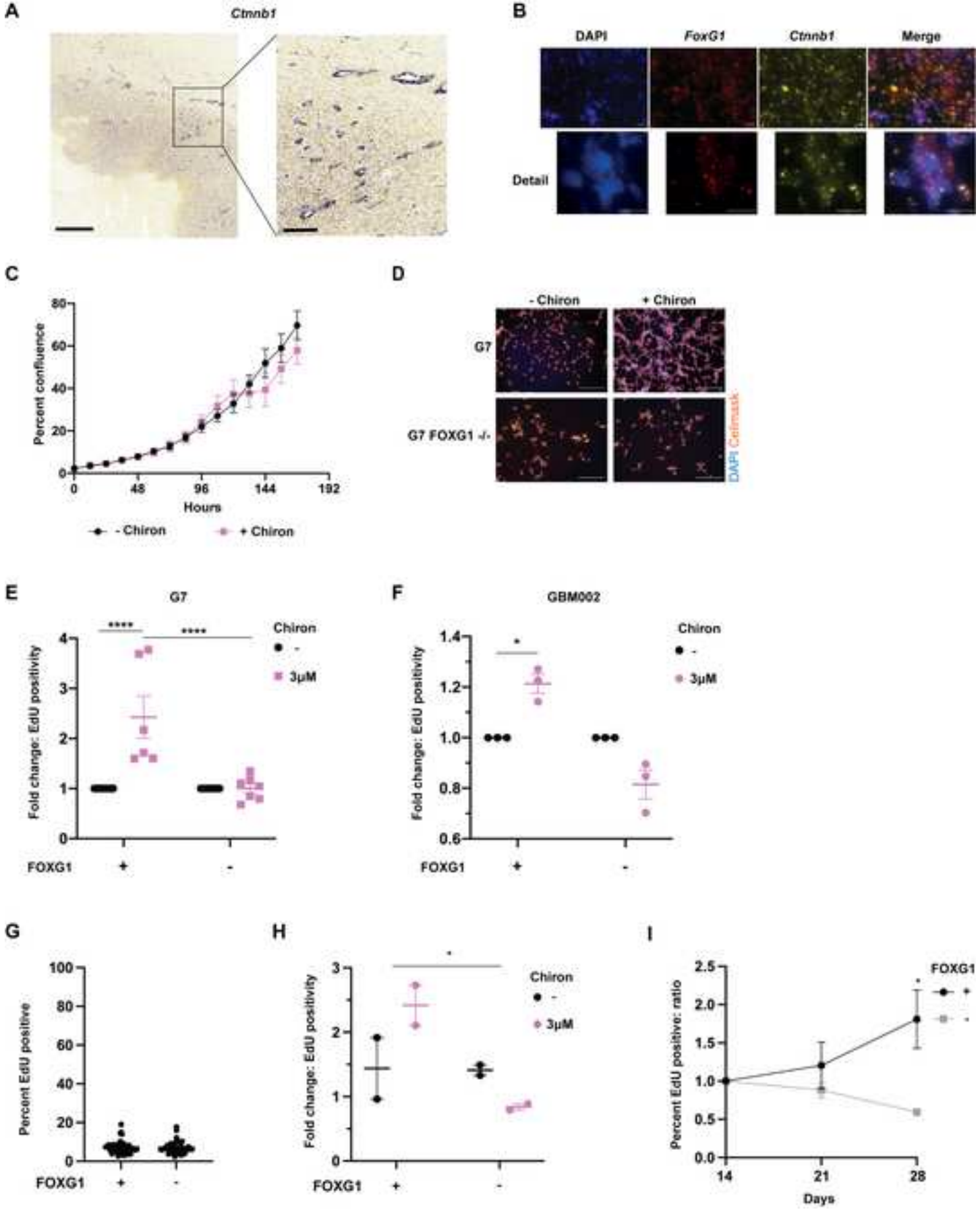

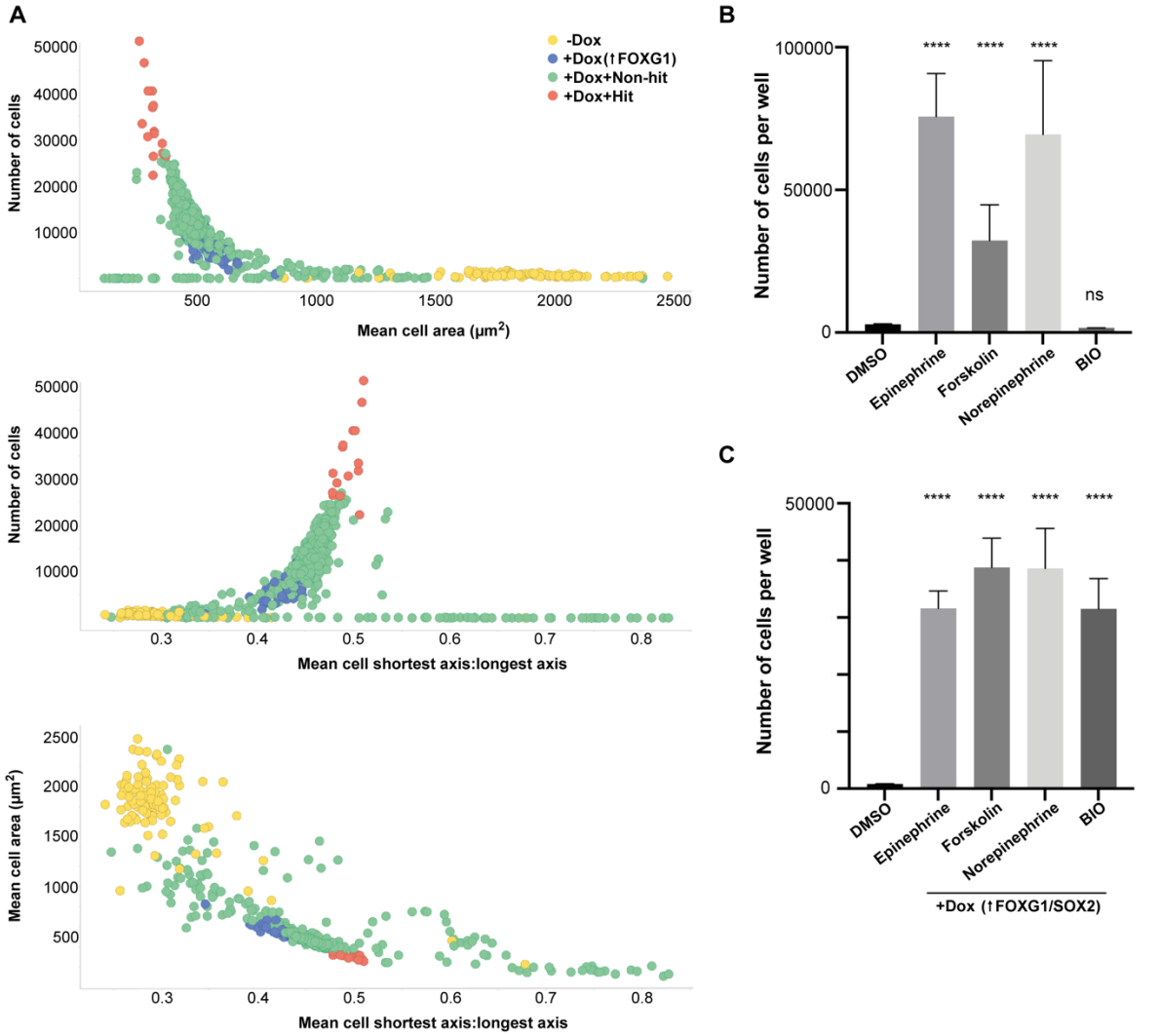

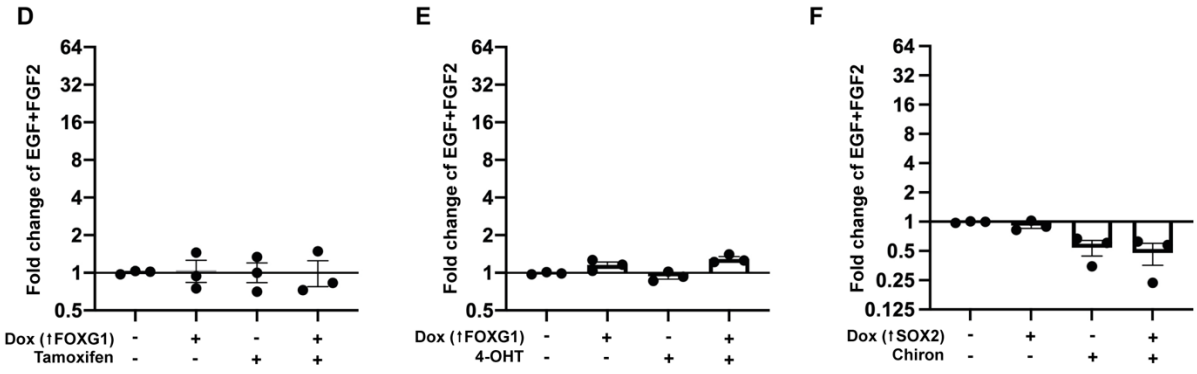

G

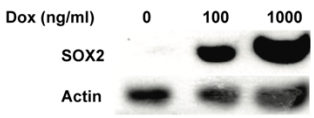

H

Mean +Dox	Mean -Dox	SD +Dox	SD -Dox	Z'
10477.27	1729.733	2629.409	435.2303	0.246832
8803.5	1858.767	2153.094	355.0453	0.294295
2021.067	717.6	452.8303	85.91881	0.409842
1969.967	726.9333	310.7397	61.65193	0.585756

Figure S1. Screening optimisation, validation and morphology data. Related to Figure 1 | (A) Scatter plots of morphology data obtained from small molecule screen, showing distinct features of cells not exposed to Dox (larger, with long processes) and those exposed to Dox and those defined as hits. Refer also to Figure 1B, representative images. (B) Quantification of cell number for the 4 screen hits, plated in BMP4 and returned to EGF+FGF+DMSO or compound (no Dox). Performed in triplicate. One-way ANOVA with Dunnett's multiple comparison tests. Significance shown for comparison to EGF+FGF2+DMSO. (C) Quantification of cell number for the 4 screen hits, plated in BMP4 and returned to EGF+FGF+DMSO or compound (+Dox). Performed in triplicate. One-way ANOVA with Dunnett's multiple comparison tests. Significance shown for comparison to EGF+FGF2+DMSO. (D)&(E) Tamoxifen citrate and active metabolite 4-hydroxytamoxifen fail to drive cell cycle re-entry in repeat assays (BMP4 for 24 hours, return to EGF+FGF2 6 days +/- dox and/or tamoxifen). Performed in independent triplicate; >10 technical replicates each. Scale to show comparison to validated hits (Figure 1E). Non-significant. One-way ANOVA. (F) SOX2 induction and GSK3 inhibition show no increase in exit from quiescence in the absence of FOXG1 induction. Fold change in S15 cell number (cf. EGF+FGF2 alone) by condition (EGF+FGF2 +/- Dox and/or Chiron). Non-significant. One-way ANOVA. Performed in independent triplicate; >10 technical replicates each. (G) Western blot confirming upregulation of human SOX2 by doxycycline in cells with Dox-inducible SOX2 only (S15 cells). Actin is used as a loading control. (H) Z' score for 4 plates of FOD3 cells during screen optimisation. Each row represents a plate seeded using successive techniques and the Multidrop Combi reagent dispenser (ThermoFisher).

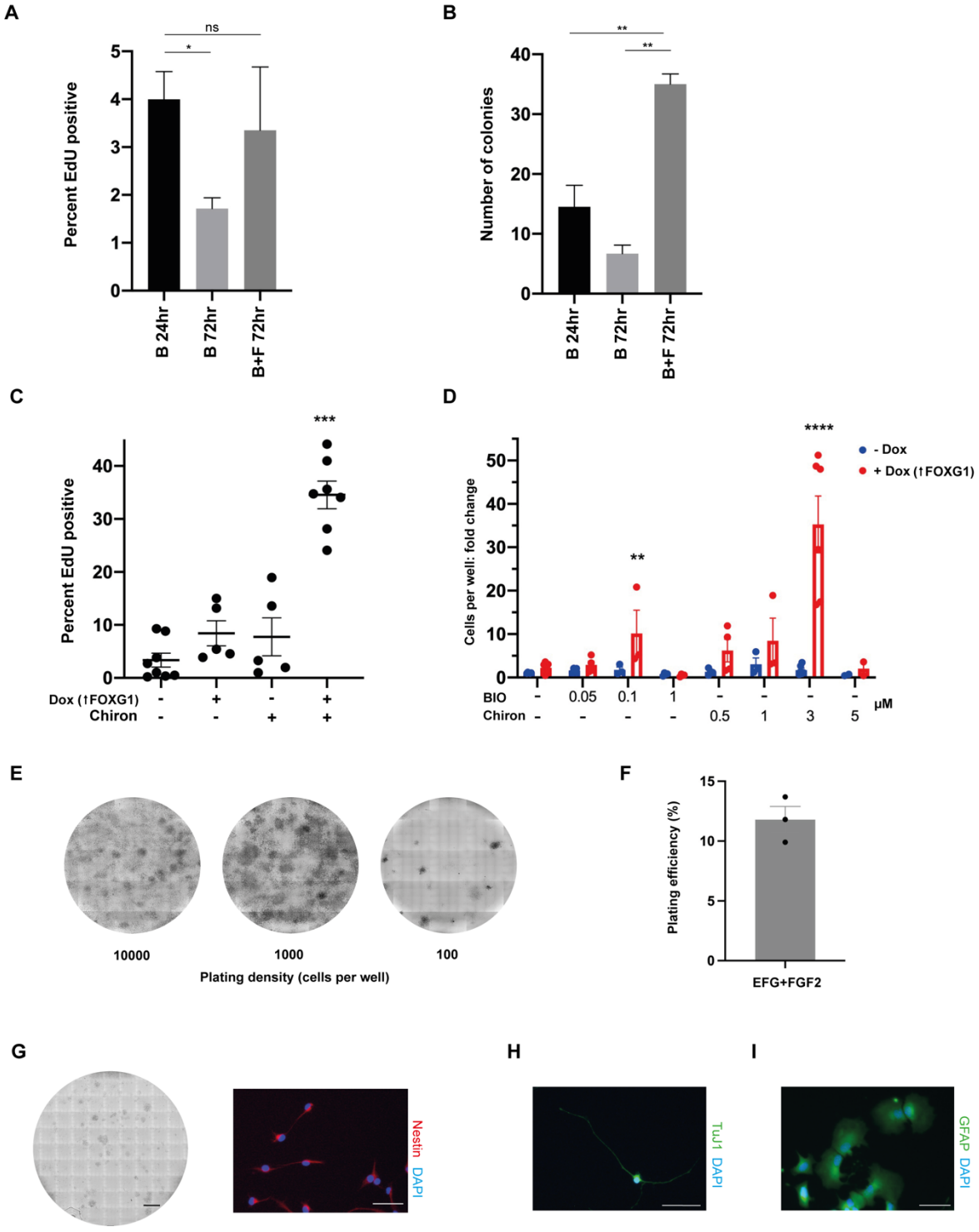

Figure S2. Confirmation of synergy between FOXG1 and GSK3 inhibition. Related to Figure 2 | (A) Quantification of EdU incorporation in F6 after exposure to BMP4 for 24 hr (B24hr) or 72 hr (B72hr) or to BMP4+FGF2 for 72hr (B+F72hr) then to EGF+FGF2 for 4 days, showing minimal EdU incorporation in all conditions. One-way ANOVA with Tukey's multiple comparison tests. Performed in triplicate. One-way ANOVA with Tukey's multiple comparison tests. (B) Quantification of colony formation in F6 after exposure to BMP4 for 24 hr (B24hr) or 72 hr (B72hr) or to BMP4+FGF2 for 72hr

(B+F72hr) then to EGF+FGF2 for 10 days. Means of 3-6 replicates. One-way ANOVA with Tukey's multiple comparison tests. (C) EdU incorporation after 72hr BMP4+FGF2 and return to mitogens +/- Dox and/or Chiron for 4-6 days, comparable to the equivalent assay with 24hr BMP4 exposure (Figure 2B). n=8 independent replicates; 15 technical replicates each. Kruskal-Wallis test with Dunn's multiple comparison tests. Significance for comparison to EGF+FGF2 shown. (D) Increase in F6 cell number after BMP4 exposure for 24hr and return to EGF+FGF2 alone or with varying doses of BIO or Chiron +/- Dox for 6 days. Two-way ANOVA. Significance in comparison to EGF+FGF2 alone shown. n=6 independent replicates; >3 technical replicates each. (E) Representative images of serial dilution colony assays: 10000, 1000, 100 cells plated per well (6 well plate) in BMP4 with return to EGF+FGF2+Dox+Chiron for 10 days. Scale bars 2mm. (F) Quantification of colony forming efficiency (% of cells plated which give rise to colonies) for F6 cells plated in EGF+FGF2 and never exposed to BMP4. n=3. (G) Representative image of colony formation from serially passaged F6 cells following Dox+Chiron exposure. Scale bar 1cm. Representative image of Nestin expression in cells in this assay. Scale bar 50μm. DAPI, blue; Nestin, red. Cells were plated at 100 cells/well in 6 well plates in BMP4 media, then changed to EGF+FGF2 + Dox + Chiron after 24 hours. After 8 days, colonies had formed and these were picked and replated in EGF+FGF2 in 6 well plates at low density. After 2 weeks, colonies had formed and these were replated in EGF+FGF2 media in 10cm dishes at low density. After 2 weeks, plates were fixed and either stained with methylene blue and imaged on the Celigo Image Cytometer (Nexcelom) or subjected to immunocytochemistry for Nestin. (G&H) Representative images of F6 cells. Cells were plated at 100 cells/well in 6 well plates in BMP4 media, then changed to EGF+FGF2 + Dox + Chiron after 24 hours. After 8 days, colonies had formed. Media was changed to either 10% fetal calf serum for 5 days (for astrocyte differentiation assay, G) or FGF2 media (withdrawal of EGF) for 24 hours, then media without growth factors for 7 days (for neuronal differentiation assay, H). Scale bars 50μm.

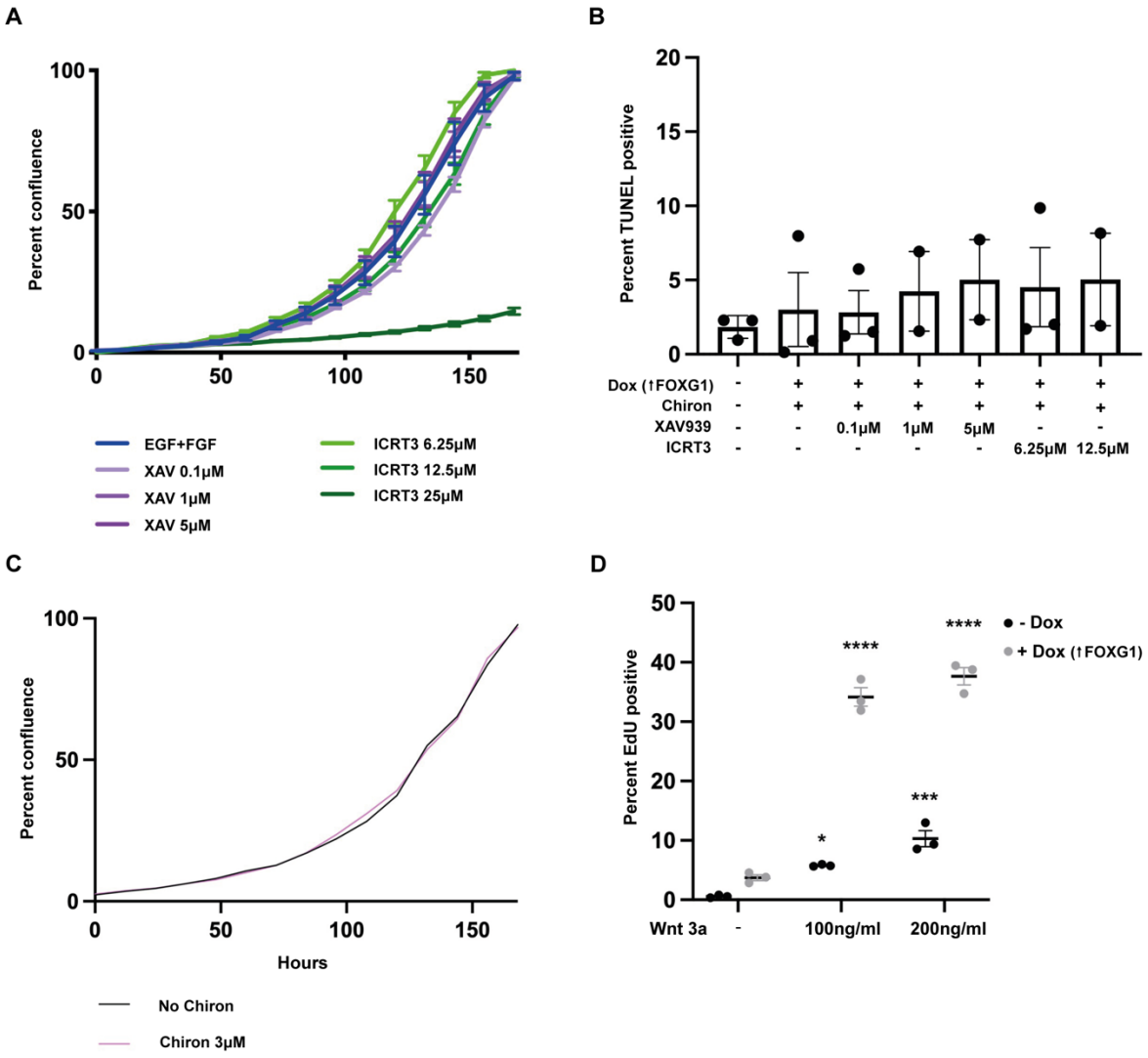

Figure S3. Wnt activation and inhibition confirm Wnt pathway involvement in the synergy with FOXG1 on quiescence exit; Wnt activation is not essential for proliferation. Related to Figure 3. (A) Growth curves showing that XAV939 has no effect on the proliferation of NSCs (F6) in EGF+FGF2 up to a concentration of 5µM and that ICRT3 has no effect on proliferation up to a dose of 12.5µM. n=6. (B) TUNEL assay confirming no significant increase in apoptosis in F6 cells with Wnt inhibitors as compared to EGF+FGF2 alone. One-way ANOVA. Performed in independent duplicate. (C) Growth curve of F6 cells plated in EGF+FGF2 +/- Chiron. (D) Quantification of EdU incorporation in F6 cells after BMP4+FGF2 72hr and return to mitogens +/- Wnt3a +/- Dox for 4 days (at this timepoint, cell number changes were minimal). Two-way ANOVA. Performed in independent triplicate; 6 technical replicates each.

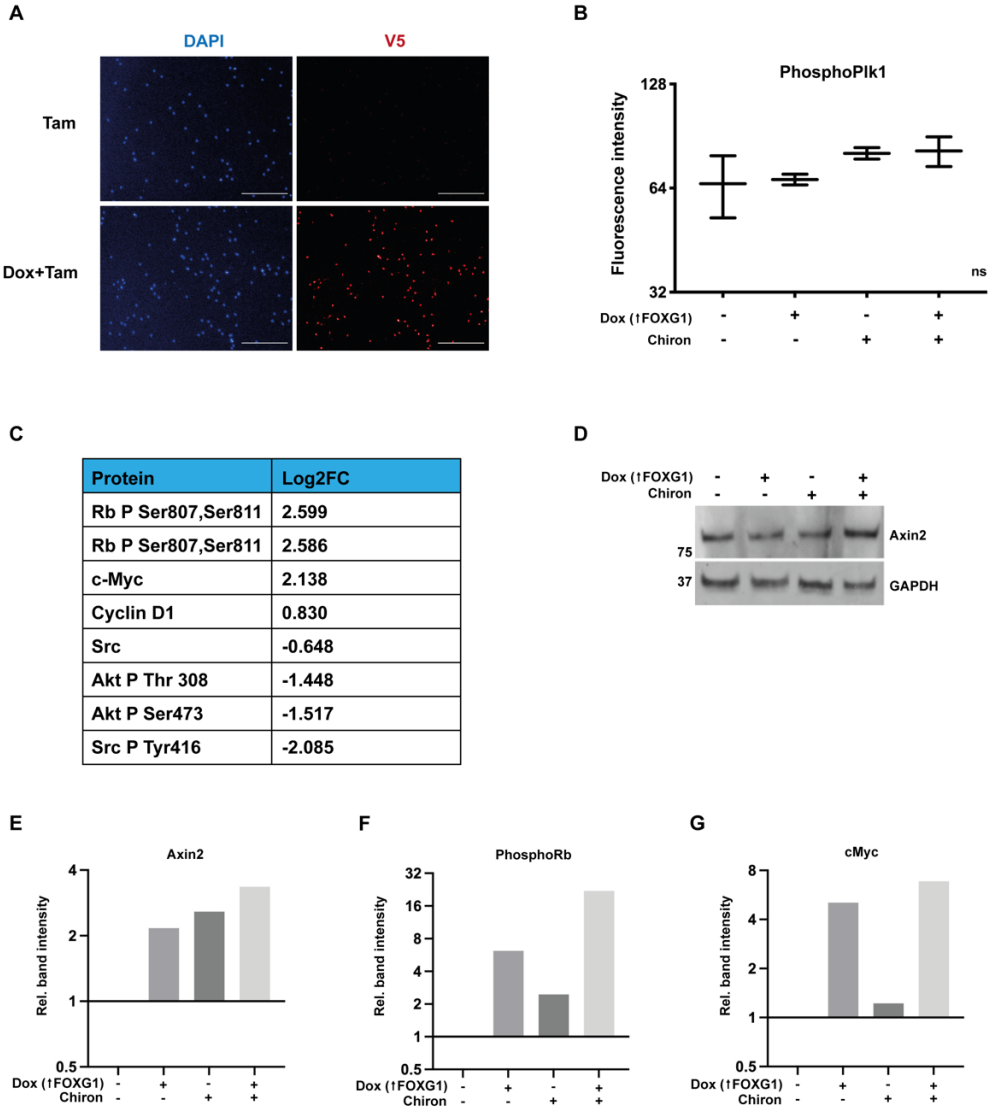

Protein	Log2FC
Rb P Ser807,Ser811	2.599
Rb P Ser807,Ser811	2.586
c-Myc	2.138
Cyclin D1	0.830
Src	-0.648
Akt P Thr 308	-1.448
Akt P Ser473	-1.517
Src P Tyr416	-2.085

Figure S4. Additional data pertaining to RPPA and to the F6BC1 line. Related to Figure 4. (A) V5 staining (red) confirms that the inducible FOXG1 cassette is intact in the F6BC1 cell line and that it is not activated by tamoxifen. Blue – DAPI. Scale bars 150μm. (B) Relative levels of mitotic marker phosphoPlk1 showing no significant difference between the 4 conditions in the RPPA assay. Kruskal-Wallis test. Data plotted are medians of 4 serially diluted dots from 3 technical replicates of independent duplicates. (C) Table of all significant hits (T-tests with Holm-Sidak correction, cut off p value <0.05) from RPPA with Log2 fold change in fluorescence intensity between EGF+FGF2 samples and EGF+FGF2+Dox+Chiron samples. (D) Western blot for Axin2 in F6 cells exposed to BMP4 for 24hr and then to EGF+FGF2 +/- Dox and/or Chiron for 2 days. (E) Quantification of band intensity for the blot shown in panel D, normalized to GAPDH. Quantified with ImageJ software. (F&G) Quantification of band signal for the Western blot shown in Figure 4G. Quantified with ImageJ software.

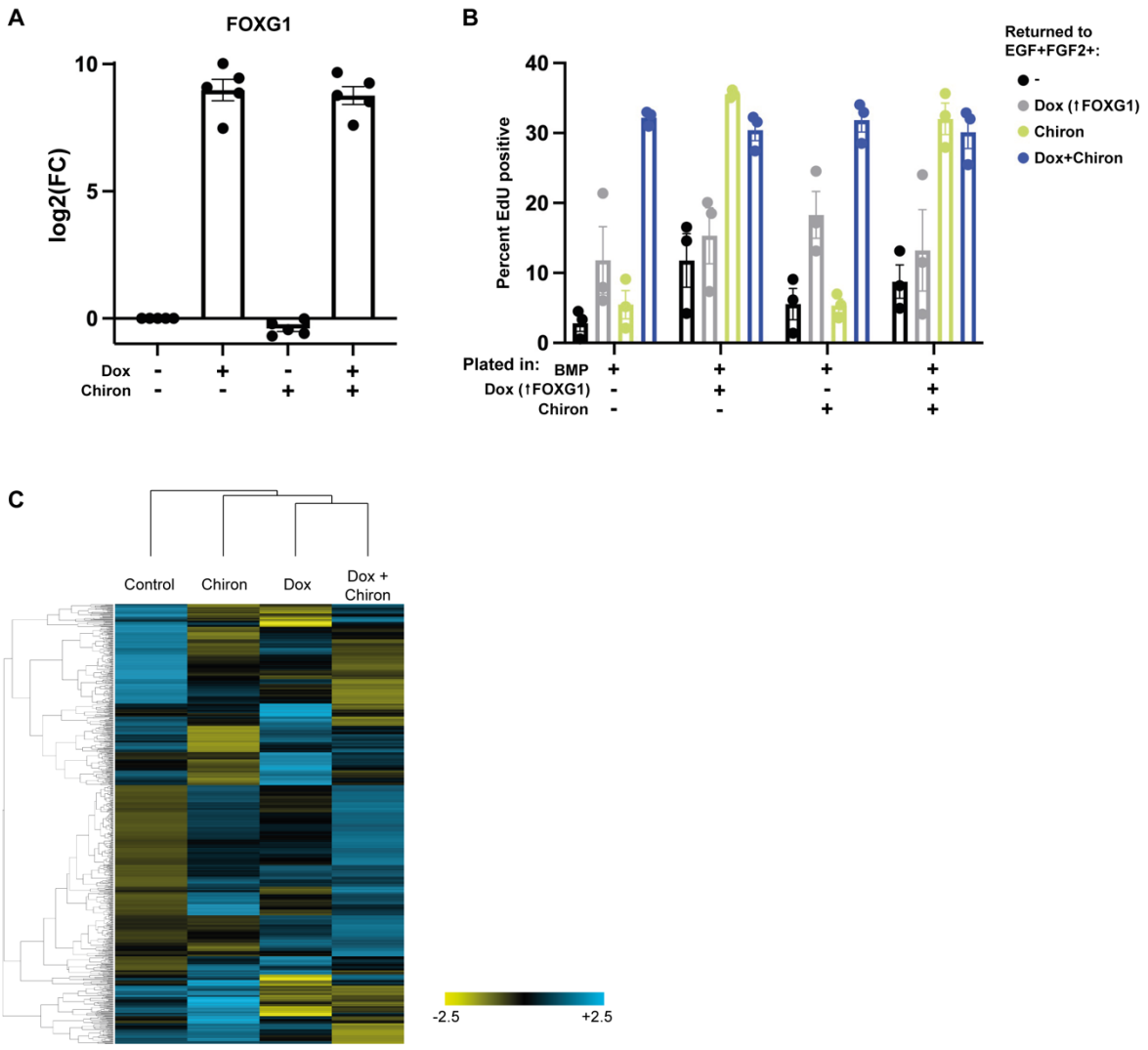

Figure S5. FOXG1 primes cells to respond to GSK3 inhibition; additional data pertaining to Nanostring in F6. Related to Figure 5. (A) qRT-PCR in F6 cells after 72hr in BMP4+FGF2 then 72hr in EGF+FGF2 +/- Dox and/or Chiron shows that human FOXG1 is elevated to similar levels in Dox and Dox+Chiron, as expected. n=5 independent replicates; 3 technical replicates each. (B) EdU incorporation in F6 cells after exposure to BMP4 +/- Dox and/or Chiron shows that Dox (induction of FOXG1 overexpression) during BMP4 exposure primes cells to exit quiescence in response to Chiron, resulting in similar exit from quiescence, in primed cells, to Dox+Chiron. n=3 independent replicates; 3 technical replicates each. (C) Heatmap of NanoString data.

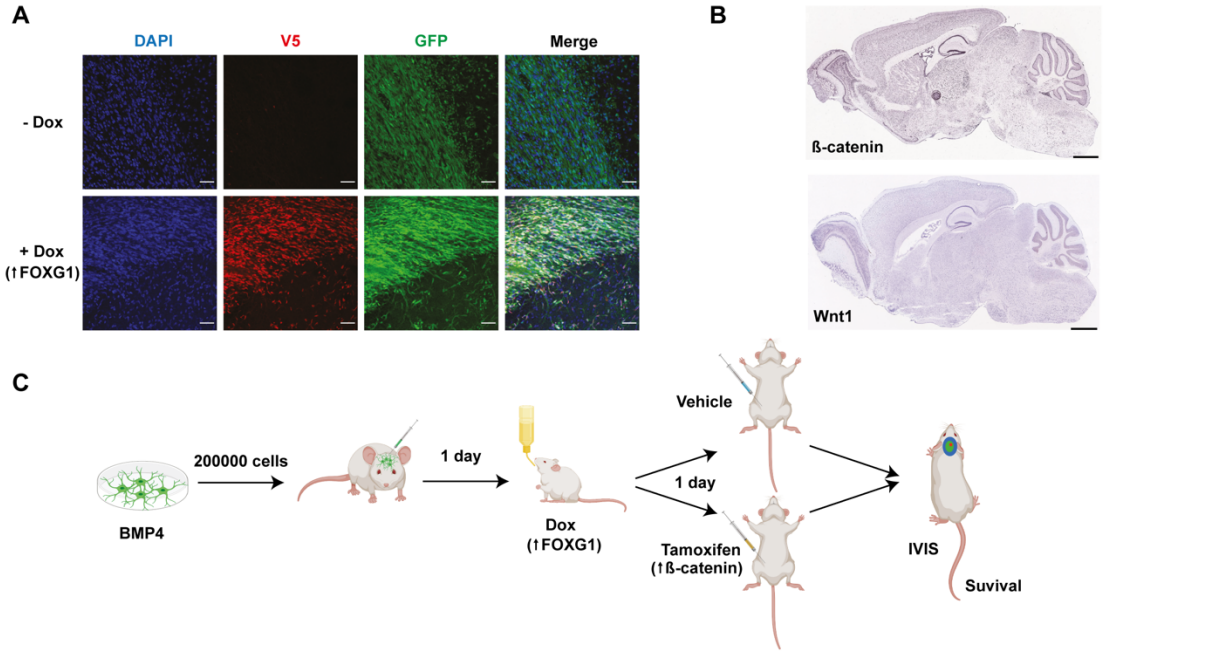
A
DAPI
V5
GFP
Merge
- Dox
+ Dox
(↑FOXG1)
B
ß-catenin
Wnt1
C
200000 cells
BMP4
1 day
Dox
(↑FOXG1)
1 day
Vehicle
Tamoxifen
(↑ß-catenin)
IVIS
Suvival
D
4 weeks
+ Dox only
(↑FOXG1)
+ Dox + Tam
(↑FOXG1,
↑ß-catenin)
5 weeks
+ Dox only
(↑FOXG1)
+ Dox + Tam
(↑FOXG1,
↑ß-catenin)
E
DAPI
GFP
ß-catenin
Merge
- Dox
+ Dox
(↑FOXG1)
F
DAPI
GFP
Ki67
Merge
- Dox
+ Dox
(↑FOXG1)
G
Percent Ki67 positive
20
15
10
5
0
Dox
-
+
H
Wif1
Mean gray value
7000
6000
5000
4000
3000
Dox
-
+

Figure S6. Additional data pertaining to in vivo findings. Related to Figure 6. (A) Representative images showing GFP positive tumour cells generated from F6BC1NPE cells, showing expression of V5 in the context of Dox administration. Blue – DAPI, red – V5, green – GFP. Scale bars 50μm. (B) ISH for Ctnnb1 and Wnt 1 in the adult mouse brain, mouse.brain-map.org. Scale bar 1250μm. (C) Schematic of the experiment used to evaluate the impact of tamoxifen on tumour growth in this model. Created with BioRender. (D) IVIS images at 4 and 5 weeks for mice (cohort 1 of 2) given Dox in drinking water +/- IP injection of Tamoxifen. (E) Representative images showing increased ß-catenin expression in the context of Dox administration in F6BC1NPE tumours in mice culled at 21 days. Blue – DAPI, red - ß-catenin, green – GFP, scale bars 50μm. Expanded image shows some cells expressing nuclear ß-catenin. (F) Representative images showing increased Ki67 expression in the context of Dox administration in F6BC1NPE tumours in mice culled at 21 days. Blue – DAPI, red – Ki67, green - GFP. Scale bars 50μm. (G) Quantification of Ki67 positivity in these tumours. (H) Quantification of Wif1 signal intensity in F6BC1NPE tumours in mice given Dox or no Dox and culled at 21 days n=8.

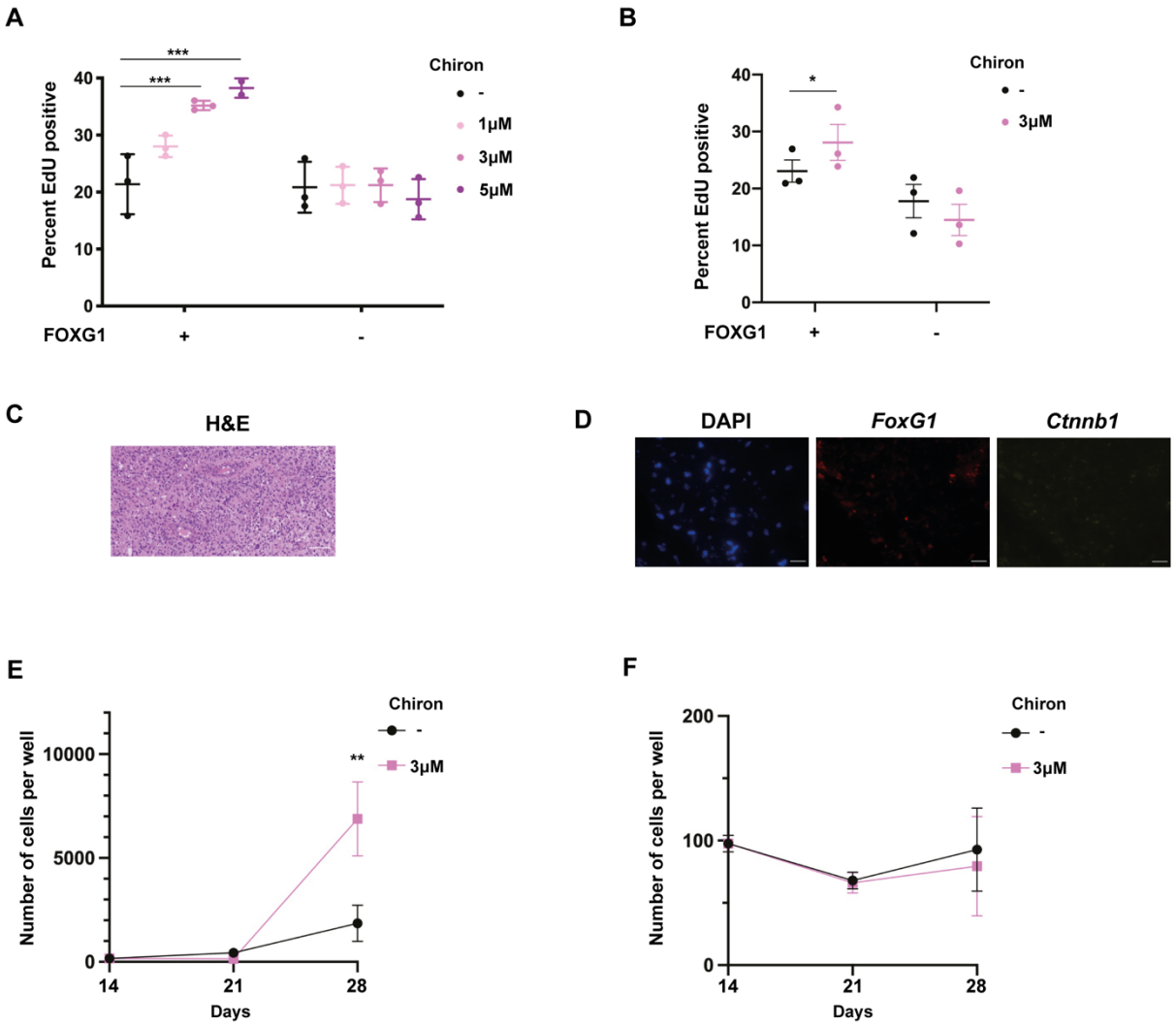

Figure S7. Additional data pertaining to the findings in human GSCs. Related to Figure 7. (A&B) Quantification of EdU incorporation in (A) G7 and G7 FOXG1 KO cells and in (B) GBM002 and GBM002 KO cells, showing that Chiron drives exit from quiescence in a dose-dependent manner, only in the context of intact FOXG1. Two-way ANOVA with Sidak's multiple comparison tests. n=3 independent replicates; 15 technical replicates each. (C) Haematoxylin and eosin stain of patient GBM sample G313. Scale bar 100 μm (D) Representative images of RNAScope peformed on G313 with negative control probes. DAPI, blue; *FoxG1* mRNA, red; *Ctnnb1* (ß-catenin) mRNA, yellow. Scale bars 50 μm. (E&F) Cell number per well in (E) GBM002 and (F) GBM002 FOXG1KO cells plated at 1000 cells/well at day -1 and irradiated at day 0 with 8Gy. Chiron or DMSO control added to media at day 14, n=6-12. Linear regression analysis.

Mean +Dox	Mean -Dox	SD +Dox	SD -Dox	Z’
10477.27	1729.733	2629.409	435.2303	0.246832
8803.5	1858.767	2153.094	355.0453	0.294295
2021.067	717.6	452.8303	85.91881	0.409842
1969.967	726.9333	310.7397	61.65193	0.585756

Table S1. Z’ score for 4 plates of FOD3 cells during screen optimisation. Each row represents a plate seeded using successive techniques and the Multidrop Combi reagent dispenser (ThermoFisher

Gene mRNA	Log2FC	Gene mRNA	Log2FC	Gene mRNA	Log2FC	Gene mRNA	Log2FC	Gene mRNA	Log2FC	Gene mRNA	Log2FC	Gene mRNA	Log2FC
Wif1	-4.23	Map2k1	-1.49	Acvr2a	-1.05	Sos2	-0.716	Acvr1b	-0.48	Atr	0.543	Rfc4	1.27
Map3k5	-3.57	Cacnb2	-1.47	Id1	-1.04	Tiam1	-0.715	Aph1b	-0.473	Rad50	0.656	Ets2	1.35
Hmga2	-2.97	Bdnf	-1.45	Ppp3ca	-1.03	Apc	-0.71	Smo	-0.472	Col5a1	0.69	Mdc1	1.38
Etv4	-2.85	Kit	-1.44	Fgfr1	-1.03	Id2	-0.705	Stag2	-0.463	Casp7	0.694	Pole2	1.39
Fos	-2.58	Mapk10	-1.42	Smad9	-1.03	Pold4	-0.701	Them4	-0.455	Npm1	0.713	Cntfr	1.4
Fn1	-2.43	Zic2	-1.39	Prkaa2	-1.03	Crlf2	-0.68	Rbx1	-0.446	Tnfrsf10b	0.744	Nasp	1.6
Il1r1	-2.34	Igf1r	-1.38	Smad3	-1.02	Capn2	-0.677	Stk11	-0.444	Fancf	0.82	Chek2	1.73
Gas1	-2.34	Gnaq	-1.38	Idh1	-1.01	Kdm6a	-0.675	Spop	-0.438	Cdkn2d	0.849	Efna2	1.81
Gpc4	-2.33	Lef1	-1.37	Pbx3	-1.01	Abl1	-0.659	Fbxw11	-0.437	Hmga1	0.857	H2afx	1.84
Pdgfc	-2.29	Itga6	-1.36	Pik3ca	-0.995	Mapk8ip1	-0.65	Ppp3r1	-0.429	Shc4	0.893	E2f1	1.87
Dusp6	-2.26	Mllt3	-1.3	Rras2	-0.993	Pld1	-0.65	Mapk3	-0.416	Ezh2	0.893	Brca1	2.22
Spry1	-2.17	Gadd45g	-1.3	Prkar2a	-0.982	Idh2	-0.641	Smad4	-0.407	Rac3	0.911	Mcm7	2.22
Ptch1	-2.1	Tnfaip3	-1.3	Nfkbia	-0.964	Wnt5b	-0.638	Kras	-0.407	Cdkn1a	0.927	Pold1	2.28
Nog	-2.1	Skp1a	-1.3	Ppp2cb	-0.963	Irs1	-0.631	Ikbkb	-0.403	Cacnb3	0.961	Rad51	2.3
Kitl	-2.06	Prkca	-1.3	Bcl2l1	-0.948	Rac1	-0.63	Chuk	-0.374	Blm	0.962	Ccne1	2.42
Fgf12	-2.06	Cdkn1b	-1.28	Lifr	-0.947	Braf	-0.627	Bap1	-0.373	Myc	0.974	Hist2h3b	2.46
Nfkbiz	-2.03	Ptk2	-1.27	Egfr	-0.943	Nfatc1	-0.623	Prkaca	-0.372	Fen1	0.981	Hist1h3b	2.47
Spry	-2.02	Irak2	-1.26	Jak2	-0.939	Mapk9	-0.62	Sos1	-0.364	Wee1	0.982	Hells	2.6
Casp12	-2.01	Gadd45a	-1.23	Hspa2	-0.938	Endog	-0.617	Grb2	-0.362	Tgfb3	0.985	Ube2t	2.65
Gng12	-2.01	Wnt5a	-1.22	Xrcc4	-0.932	Stat1	-0.611	Ppp2r1a	-0.353	Cacna1h	0.986	Nkd1	2.74
Fgf1	-1.96	Zbtb16	-1.22	Fzd3	-0.911	Jak1	-0.598	Smarcb1	-0.341	Hes1	0.989	Mcm2	2.75
Itgb8	-1.94	Igfbp3	-1.2	Nfkb1	-0.901	Stat3	-0.598	Mtor	-0.34	Cdc25a	0.989	Stmn1	2.82
Six1	-1.82	Casp3	-1.18	Mllt4	-0.887	Nfe2l2	-0.59	Arnt2	-0.327	Atm	1.04	Socs2	2.86
Plcb4	-1.79	Gnas	-1.15	Nf2	-0.883	Xpa	-0.586	Ifnar1	-0.319	Cdk2	1.05	Chek1	2.91
Tspan7	-1.79	Insr	-1.14	Tcf7l1	-0.882	Rhoa	-0.576	Mapk1	-0.293	Efna3	1.07	Ccne2	3.15
Ppargc1a	-1.78	Map3k1	-1.14	Etv1	-0.849	Map2k4	-0.575	Alkbh3	-0.27	Skp2	1.08	Top2a	3.27
Cacnb4	-1.77	Ifnar2	-1.12	Mnat1	-0.841	Dvl3	-0.571	Map3k7	-0.24	Bmp7	1.1	Mcm5	3.32
Hist2h3c2	-1.76	Cyld	-1.11	Camk2b	-0.812	Hdac4	-0.569	Smarca4	0.157	Axin2	1.14	Ttk	3.68
Cd14	-1.71	Angpt2	-1.11	Cdkn2c	-0.791	Cul1	-0.557	Fubp1	0.352	Suv39h2	1.2	Il6ra	3.77
Fut8	-1.61	Shc3	-1.09	Smad1	-0.774	Ccnd2	-0.557	Cdk4	0.472	Dnmt1	1.21	Ccna2	4.03
Hspa1a	-1.59	Fzd7	-1.09	Maml2	-0.75	Mlh1	-0.556	Tfdp1	0.519	Cdc7	1.21	Cdc25c	4.32
Ikbkg	-1.51	Tlr4	-1.09	Prkacb	-0.742	Foxo4	-0.504	Rfc3	0.527	Pcna	1.23		
Bambi	-1.5	Map3k8	-1.08	Hsp90b1	-0.717	Rpa3	-0.497	Dnmt3a	0.539	Mcm4	1.24		

Table S1. Table of all significant hits from NanoString with Log2 fold change in count between EGF+FGF2 samples and EGF+FGF2+Dox+Chiron samples. (Statistics using NSolver Advanced Analysis software as per Wang et al, 2016, cut off p value <0.0

Trp53_L, sgRNA	Gangoso et al[40], Integrated DNA Technologies	GCTGGCAGAATAGCTTATTG
Trp53_R, sgRNA	Gangoso et al[40], Integrated DNA Technologies	GAGCGCAAAGAGAGGTACGC
Pten_L, sgRNA	Gangoso et al[40], Integrated DNA Technologies	GGTTTGATAAGTTCTAGCTG
Pten_R, sgRNA	Gangoso et al[40], Integrated DNA Technologies	GTAAATACGTTCTTCATACC
Nf1_L, sgRNA	Gangoso et al[40], Integrated DNA Technologies	TCATCATCACATCTTCGGAT
Nf1_R, sgRNA	Gangoso et al[40], Integrated DNA Technologies	TCGGCTGCTTTGGAACAATC
hEGFRvIII_Fwd primer	Gangoso et al[40], Sigma	ATCACAAGTTTGTACAATGCGACCCTC CGGGACGGCC
hEGFRvIII_Rev primer	Gangoso et al[40], Sigma	CACCACTTTGTACATCATGCTCCAATAA ATTCACT
3FLAG-LUC-2AGFP Fwd primer	Gangoso et al[40], Sigma	GGGGACAAGTTTGTACAAAAAAGCAGG CTTCGCCACCATGGACTACAAAGA

3FLAG-LUC-2AGFP Rev	Gangoso et al[40], Sigma	GGGGACCACTTTGTACAAGAAAGCTGG GTTTTACTTGTACAGCTCGTCCA
FOXG1 sgRNA-1	Bulstrode et al[19], Sigma	CCGCCCTGGACGGGGCTAA
FOXG1 sgRNA-2	Bulstrode et al[19], Sigma	GCAAGGGCGAGCCGGGCGG
Foxo3_gRNA1	Bulstrode et al[19], Sigma	CGCGTTCAGAATGAAGGCACGGG
Foxo3_gRNA2	Bulstrode et al[19], Sigma	CGCATGAAGCGGCTGTGCAGGG

Table S2. Oligonucleotides.